Parameterized level-set based pharmacokinetic fluorescence optical tomography using the regularized Gauss-Newton filter

Omprakash Gottam[a], **Naren Naik**[a,b,*], **Sanjay Gambhir**[c]
[a]Department of Electrical Engineering, Indian Institute of Technology Kanpur, INDIA, 208016
[b]Center for Lasers and Photonics, Indian Institute of Technology Kanpur, INDIA, 208016
[c]Department of Nuclear Medicine, Sanjay Gandhi Postgraduate Institute of Medical Sciences, INDIA, 226014

Abstract. Pharmacokinetic tomography is emerging as an important methodology of detecting abnormalities in tissue based upon spatially varying estimation of the pharmacokinetic rates governing the leakage of an injected fluorophore between blood plasma and tissue. We present a shape-based reconstruction framework of a compartment-model based formulation of this dynamic fluorescent optical tomography (FOT) problem, to solve for the pharmacokinetic rates and concentrations of the fluorophore from time-varying log intensity measurements of the optical signal. The compartment-model based state variable model is set up in a radial basis function (RBF) parameterized level set (PALS) setting. The state (concentrations) and (pharmacokinetic) parameter estimation problem is solved with an iteratively regularized Gauss-Newton filter in a trust-region framework. Reconstructions obtained using this scheme for noisy data obtained from cancer mimicking numerical phantoms of near/sub-cm sizes, show a good localization of the affected regions and reasonable estimates of the pharmacokinetic rates and concentration curves.

Keywords: Pharmacokinetic tomography, fluorescence optical tomography, level-set based reconstructions, parameterized level sets, regularized Gauss-Newton filter, early cancer detection, functional imaging.

*Naren Naik, nnaik@iitk.ac.in

1 Introduction

The detection of early cancer requires the capturing of physiological changes that occur in the affected cells before their structure/morphology changes. Tomographic modalities that capture the tell-tale biochemical/physiological signatures of early cancer are nuclear medicine based schemes such as positron emission tomography (PET) or optical tomography based ones such as fluorescence optical tomography (FOT). Two kinds of information that can be inferred about the region of interest from these modalities are the absorption (concentration) distribution of introduced markers (that attach themselves to the affected regions), and, the rates at which the markers enter and leave the regions of interest.[1–14]

Pharmacokinetic rates are the parameters that govern the passage of the markers across notional compartments in the body such as blood-plasma and tissue ones.[15–17] These rates have

been found to bear the signatures of abnormalities in the tissue,[1,4,9,10,18–22] thus yielding a potentially powerful tool of early diagnosis. In FOT, pharmacokinetic-rate reconstructions have been proposed in a compartment model setting, to detect oncological abnormalities in tissue,[9,10,19–22] where a state variable model is constructed with fluorophore-concentrations being the states, and the pharmacokinetic rates and volume fractions being the parameters. In Alacam *et al.*[21] the concentrations at all points in the domain are reconstructed at each time instant from a linearized (Rytov) approximation based inversion of the complex log-intensity data at each instant. Subsequently, in a second step, at each spatial point, a state variable model using the reconstructed total concentration of the fluorophore in tissue as the measurement, is used to estimate the states (compartment-concentrations) and the pharmacokinetic parameters. The estimation process uses an extended Kalman filter (EKF) framework.

Alternatively in a one-step method, Alacam *et al.*[9] and Wang *et al.*[10] demonstrate that the use of log-intensity measurements to directly reconstruct spatially resolved compartment-concentrations and pharmacokinetic rates (rather than going via the pointwise total concentrations) offer potentially better reconstructions. Exhaustive reconstruction studies have been carried out by Alacam *et al.*[9] comparing the performance of "one-step" linear as well as nonlinear inversions, with the "two-step"[21] linearly modeled approach for diffusion-model studies in an EKF framework.

Dual mode (X-ray CT with FOT) dynamic FOT pharmacokinetic reconstructions have also been approached in one and two-step least-squares based inversions, with linear Born-approximation propagation models using compartment-model derived bi-exponential temporal solutions, with structural priors obtained from X-ray CT.[13,23–25] The structural priors better specify tissue optical properties corresponding to the organs housing various regions in the image, as well as, regularize the reconstructions.[26] In such a dual-mode setting,[12] a Karhunen-Loeve transform (KLT) based

reconstruction is first carried out with a linear Born-type measurement model for the time-varying concentrations, and then a bi-exponential temporal model is used to obtain corresponding pharmacokinetic parameters.

Shape-based tomographic reconstructions are gaining importance[27–35] in order to reduce search space dimensions and thus enhance computational tractability. A B-spline parametrization is used to represent absorption distribution in a two dimensional (2D) diffuse photon density wave model which is solved using a greedy type optimization approach.[36] An ellipsoid representation of the absorption anomalies is used in an optical tomography (OT) problem setting using the Gauss-Newton (GN) method with line search.[28] Spherical harmonic parametrization is used to represent diffusion and absorption coefficients in a three dimensional (3D) OT problem, which is then solved using a line search based GN scheme.[29] In an implicit parametrized level-set framework, Aghasi *et al*.[37] solve the diffusion optical tomography problem with radial basis function (RBF) based parametric level sets (PALS). A Hermite interpolation based RBF representation is used in a 2D FOT problem by Naik *et al*.[38] to represent the fluorophore absorption coefficient at excitation wavelength; the FOT problem is then solved in pointwise and shape-based frameworks using Levenberg-Marquardt/Gauss-Newton methods.

A dynamic optical tomography problem in straight path ray-tomography was also solved[39] using RBF level-set object-boundary representations and Gauss-Newton filter based estimation of the dynamic shape and optical parameters. Non-parameterized pointwise-specified level-sets are used to implicitly represent the boundary of time varying fluorescence yield[40] in fluorescence molecular tomography. The pointwise level-set function and the piecewise constant values of the yield for the different time instants and projection angles are reconstructed using a gradient descent method.[40] It should be noted that a state variable model is not used in the above mentioned work

to relate the fluorescent yield at different time instants.

Considering that we require spatially resolved images of various pharmacokinetic rates and volume fractions, with the objective of making the compartment model based dynamic pharmacokinetic reconstruction problem more computationally tractable, we have proposed an RBF level-set parameterized shape-based tomographic inversion scheme using a regularized trust region based Gauss-Newton filter in a diffusion-approximation modeled FOT setting. Preliminary results from such a formulation in a Levenberg-Marquardt setting have been recently presented.[41] In our pharmacokinetic tomographic settings, the (static) boundary of the tumor is reconstructed along with the dynamic concentrations within as well as the state-variable model's pharmacokinetic parameters and volume fractions. Decay of the concentrations is assured by the structure of the state ODE-model's coefficient-matrix. Hence, in order to ensure proper time-decay of concentrations we directly solve for the pharmacokinetic parameters instead of going via their exponential propagator matrix components (designated as "interim kinetic parameters" in Wang *et al.*[10]). Suitable error metrics have been then defined and detailed numerical studies for near/sub-cm tumor-mimicking phantoms for two kinds of cancer and various data-SNRs have been presented and quantified with respect to the metrics. We see that our scheme yields a good localization of the test-objects and reasonable estimates of the pharmacokinetic rates and concentration profiles.

The present paper differs from our recently presented work[41] in that: (a). The detailed formulation and derivation of the GN-filter Jacobians have been given in the present manuscript, (b) the details of the trust-region based regularized Gauss-Newton filter proposed have been given, and, (c) error metrics have now been defined, and detailed numerical studies have now been included for tumor-mimicking phantoms of two different kinds of cancer (invasive ductal carcinoma and adenocarcinoma) for various noise levels in the data and importantly the results have been well

quantified by the error-metrics.

In section 2 we discuss the compartment analysis of pharmacokinetics and shape reresentation of the states and parameters. Section 3 presents the proposed trust-region based iteratively regularized Gauss-Newton filter for the dynamic reconstruction as well as the Frechet derivatives of the measured log-intensity of the emission fluence with respect to pharmacokinetic and shape parameters. Section 4 contains the numerical studies on test-cases of typical tumor mimicking phantoms, followed by the summary in section 5. The appendix gives the expressions for the interim kinetic parameters in terms of the pharmacokinetic parameters.

2 Problem definition

2.1 State variable model for pharmacokinetic compartment analysis

Compartment modelling of pharmacokinetics is used in imaging studies[9,19,21,42–44] for cancer detection. In compartment analysis, the region of interest is divided into virtual compartments or volumes where the fluorophore concentration reaches rapid equilibrium upon injection.[16,45] Indocyanine green (ICG) is an optical contrast agent, widely used for cancer detection studies.[46–48] A two compartment model (schematic in figure 1) has been reported to be suitable for describing ICG pharmacokinetics.[44] ICG administered intravenously into blood stream binds to plasma proteins (albumin) and acts as a macromolecular agent.[43,46] Due to high leaky vasculature in tumor region,[43,49] the macromolecule leaks into cancerous tissue, absorbs the incident light at excitation wavelength and emits (fluorescent) light at a longer wavelength hence acting as a contrast agent for identifying tumors. The pharmacokinetic rates between the (blood) plasma compartment and the (tissue) Extracellular and Extravascular space compartment (EES) is higher in the tumor region due to the leaky nature of blood vessels there.

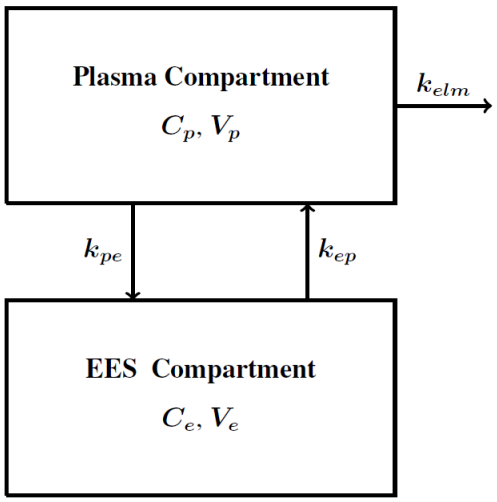

Fig 1 Block Diagram of two compartment model

The fluorophore's volume of distribution of a compartment is the apparent volume into which a given mass of fluorophore needs to be diluted in order to give the observed concentration.[50] As the contrast agent is leaked into the EES compartment, the apparent volume of distribution of ICG is more in the tumor region, than in the healthy region. Thus, due to angiogenesis, defining the volume fractions of a compartment ($v_{e/p}$) as the ratio of its volume of distribution ($V_{e/p}$) and the total volume of distribution ($V = V_e + V_p$), we see that the volume fraction of ICG in both compartments is greater in the tumor region.[43,44,51] In the tumor regions, v_e is in the range 0.2 to 0.5,[52] whereas v_p is in the range 0.013 to 0.067.[43,44]

Let $C_p\ (\mu M)$, $C_e\ (\mu M)$ be the concentration of ICG in the plasma compartment and EES compartment respectively, $k_{pe}\ (s^{-1})$ (respectively $k_{ep}\ (s^{-1})$) is the transfer rate of ICG from the plasma compartment to the EES compartment (respectively the transfer rate of ICG from the EES compartment to the plasma compartment), $k_{elm}\ (s^{-1})$ is the transfer rate at which ICG is eliminated from the region of interest.

The change in concentration of ICG in each compartment is described by the coupled ordinary

differential equations[9] (ODE)

$$\dot{\mathbf{C}}(\vec{r},t) = \mathbf{K}(k_{pe}(\vec{r}), k_{ep}(\vec{r}), k_{elm}(\vec{r}))\mathbf{C}(\vec{r},t) \tag{1}$$

where $'\vec{r}'$ denotes spatial coordinates and $\mathbf{C}(\vec{r},t) = \begin{bmatrix} C_e(\vec{r},t) \\ C_p(\vec{r},t) \end{bmatrix}$;

$\mathbf{K}(k_{pe}(\vec{r}), k_{ep}(\vec{r}), k_{elm}(\vec{r})) = \begin{bmatrix} -k_{ep}(\vec{r}) & k_{pe}(\vec{r}) \\ k_{ep}(\vec{r}) & -(k_{pe}(\vec{r}) + k_{elm}(\vec{r})) \end{bmatrix}$

The corresponding discrete time state model corresponding to time instants t_j and t_{j+1} (indexed as j and $j+1$ respectively) for (1) is given by[9,53]

$$\mathbf{C}(\vec{r}, j+1) = \mathbf{T}(\tau_{11}(\vec{r}), \tau_{12}(\vec{r}), \tau_{21}(\vec{r}), \tau_{22}(\vec{r}))\mathbf{C}(\vec{r}, j) \tag{2}$$

where

$$\mathbf{T} \equiv e^{\mathbf{K}t_s} \equiv \begin{bmatrix} \tau_{11}(\vec{r}) & \tau_{12}(\vec{r}) \\ \tau_{21}(\vec{r}) & \tau_{22}(\vec{r}) \end{bmatrix} \tag{3}$$

and $t_s = t_{j+1} - t_j$ is the sampling interval.

Denoting by subscripts 'x' and 'm' excitation and emission related quantities respectively, the frequency domain governing equations which describe light propagation in tissue are given by[54]

$$\begin{aligned} -\nabla \cdot (D_x \nabla \Phi_x) + k_x \Phi_x &= S_x \\ -\nabla \cdot (D_m \nabla \Phi_m) + k_m \Phi_m &= \beta \Phi_x \end{aligned} \qquad \text{in } \Omega \tag{4}$$

subject to the Robin boundary conditions

$$\begin{aligned} \vec{n} \cdot (D_x \nabla \Phi_x) + b_x \Phi_x = 0 \\ \vec{n} \cdot (D_m \nabla \Phi_m) + b_m \Phi_m = 0 \end{aligned} \quad \text{on } \partial\Omega \tag{5}$$

where,

$$\begin{aligned} D_{x/m} = \frac{1}{3(\mu_{a(x/m)i} + \mu_{a(x/m)f} + \mu'_{s(x/m)})}, \beta = \frac{\phi_q \mu_{axf}}{1 - i\omega\tau_l}, \\ b_{x/m} = \frac{1 - R_{(x/m)}}{2(1 + R_{(x/m)})},\ k_{x/m} = \frac{i\omega}{c} + \mu_{a(x/m)i} + \mu_{a(x/m)f} \end{aligned} \tag{6}$$

$'x/m'$ stands for either 'x' (excitation) or 'm' (emission), $\vec{n}$ is the outward normal to the boundary, S_x (W/cm^2) is the excitation source with modulation frequency ω (rad/s), Φ_x (W/cm^2) is the excitation fluence, Φ_m (W/cm^2) is the emission fluence, $D_{x/m}$ is the diffusion coefficient at excitation/emission wavelength, $k_{x/m}$ is a decay coefficient, $\mu_{a(x/m)i}$ and $\mu_{a(x/m)f}$ being the absorption coefficients due to intrinsic chromophores and extrinsic fluorophores respectively, $\mu'_{s(x/m)}$ being the respective reduced scattering coefficient, (all in cm^{-1}) at the two wavelengths, β and ϕ_q being the unitless emission source coefficient and fluorescence quantum efficiency respectively, τ_l fluorescence lifetime(in s), c is speed of light in the medium (cm/s), $i = \sqrt{-1}$, $b_{x/m}$ are Robin boundary coefficients, $R_{x/m}$ are the reflection coefficients. We use a frequency domain modeling of the FOT process because of the inherent advantage of such systems in time-sampling based applications especially at reasonably good data SNRs.

The measurements are the complex log-intensity (defined below) at the detector locations at excitation and emission wavelengths in general. In the present work, we focus on obtaining the

absorption coefficient of the tissue at excitation wavelength (μ_{axf}) from measured complex log-intensity at the emission wavelength.[54] We assume an *apriori* known linear relationship between μ_{axf} and μ_{amf}.[54] The measured log-intensity is:

$$\log(\Phi_m[\{\vec{r_d}\}]) \equiv \log|\Phi_m(\vec{r_d})| + i\nu(\vec{r_d}) \tag{7}$$

where $\Phi_m \equiv |\Phi_m(\vec{r_d})|e^{i\nu}$, and $\vec{r}_d$ denotes a detector location. Hence we can formally express the discrete-domain measurement equation at a time instant t, as:

$$y(\vec{r_d},t) \equiv \log\Phi_m[\{\vec{r_d}\},t] \equiv \mathcal{G}(\underline{\mu}_{axf}(\vec{r},t)) \tag{8}$$

where $y(\vec{r_d},t)$ represents the vector of measurements at time t, $\underline{\mu}_{axf}(t)$ the vector of unknown absorption coefficients on the computational grid at time t, and, $\mathcal{G}(\cdot)$ represents the measurement operator; in our case $\mathcal{G}(\cdot)$ is evaluated using the finite element method (FEM) for the solution of the governing fluorescence diffusion model in the equations (4,5).[54]

The relation between the total fluorophore concentration in the region of interest and the absorption coefficient is given by.[9]

$$\mu_{a(x/m)f}(\vec{r},t) = ln10 \cdot \epsilon_{(x/m)} \cdot C(\vec{r},t) \tag{9}$$

where $\epsilon_{x/m}$ is the fluorophore extinction coefficient, $C(\vec{r},t)$ is the total fluorophore concentration in the tissue and is given by[9]

$$C(\vec{r},t) = v_p(\vec{r})C_p(\vec{r},t) + v_e(\vec{r})C_e(\vec{r},t) \tag{10}$$

2.2 *Level-set representation and state variable model*

We consider a level-set based representation of a pharmacokinetic parameter k_ξ, with $\xi \in \{ep, pe, elm\}$, as

$$k_\xi(\vec{r}) = k_\xi^i(\vec{r})H(\phi_\gamma(\vec{r})) + k_\xi^o(\vec{r})(1 - H(\phi_\gamma(\vec{r}))) \tag{11}$$

where $k_\xi^i(\cdot)$ and $k_\xi^o(\cdot)$ represent $k_\xi(\cdot)$ values inside and outside the region of interest respectively. In our work, we consider k_ξ^i and k_ξ^o to be respective constants inside and outside the tumor region. H represents the Heaviside function, and $\phi_\gamma(\vec{r})$ a function whose zero level-set represents the boundary of the tumor, and whose value is positive (resp. negative) inside (resp. outside) the tumor region. γ represents a set of parameters that define this level-set. In our work we are using a radial basis function representation of the object boundary with compactly-supported parametric level sets (PALS).[37]

The compactly supported RBF level-set function can be written as[37] :

$$\phi_\gamma(\vec{r}) \equiv \phi(\vec{r}, \underbrace{[\boldsymbol{\alpha}, \boldsymbol{\zeta}, \boldsymbol{\chi}]}_{\gamma}) = \sum_{l=1}^{m} \alpha_l \psi(\|\zeta_l(\vec{r} - \chi_l)\|^\dagger) \tag{12}$$

$$\tilde{r} \equiv \|\vec{r}\|^\dagger = \sqrt{\|\vec{r}\|^2 + v^2} \tag{13}$$

v is a small real number, ψ is a compactly supported radial basis function (RBF),[55] m is the number of RBFs used, α_l is the weighting factor, ζ_l is the dilation factor, χ_l denote the RBF center coordinates.

In the present work, we use as basis functions a C^2 polynomial of degree 5[37,55]

$$\psi(\tilde{r}) = (1-\tilde{r})_+^4(4\tilde{r}+1) \tag{14}$$

where the $(\cdot)_+$ denotes a cutoff function[55] defined as:

$$(x)_+ = x \cdot H(x). \tag{15}$$

where $H(x)$ is the Heaviside function. We also use a mollified Heaviside function in our work[56]

:

$$H_\epsilon(\phi) = \begin{cases} 1 & \text{if } \phi > \epsilon_w, \\ 0 & \text{if } \phi < -\epsilon_w, \\ \frac{1}{2} + \frac{\phi}{2\epsilon_w} + \frac{1}{2\pi} sin(\frac{\pi\phi}{\epsilon_w}) & \text{if } |\phi| \leq \epsilon_w. \end{cases} \tag{16}$$

where ϵ_w is the half-width of the transition region of the Heaviside. Concentrations in different compartments C_e, C_p which are dependent on pharmacokinetic rates are similarly assumed to be piecewise constant and they can be expressed as

$$C_{(e/p)}(\vec{r}, j) = C^i_{(e/p)}(j) H_\epsilon(\phi_\gamma(\vec{r})) + C^o_{(e/p)}(j)(1 - H_\epsilon(\phi_\gamma(\vec{r}))) \tag{17}$$

The volume fractions v_e and v_p being different in healthy and tumor regions can also be similarly expressed via their inside/outside values denoted as $v_e^{i/o}$ and $v_p^{i/o}$ respectively, as:

$$v_{(e/p)}(\vec{r}) = v^i_{(e/p)}(\vec{r}) H_\epsilon(\phi_\gamma(\vec{r})) + v^o_{(e/p)}(\vec{r})(1 - H_\epsilon(\phi_\gamma(\vec{r}))) \tag{18}$$

Substituting the level-set representation of concentrations and volume fractions in the above

equation (for relation between μ_{axf} and C), we obtain

$$\mu(\vec{r},j) = ln10\cdot\epsilon\cdot[(C_e(\vec{r},j)v_e(\vec{r})+C_p(\vec{r},j)v_p(\vec{r}))] = ln10\cdot\epsilon\cdot[(C_e(j)^i v_e^i + C_p^i(j)v_p^i)H_\epsilon(\phi_\gamma(\vec{r}))+ (C_e^o(j)v_e^o + C_p^o(j)v_p^o)(1-H_\epsilon(\phi_\gamma(\vec{r})))] \quad (19)$$

where the subscripts on μ and ϵ have been omitted for ease of notation.

Using the level-set representation of pharmacokinetic rates and concentrations, the coupled ODE (1) is rewritten as

$$\begin{bmatrix} \dot{C_e}^i(t) \\ \dot{C_p}^i(t) \end{bmatrix} H_\epsilon(\phi_\gamma(\vec{r}))+ \begin{bmatrix} \dot{C_e}^o(t) \\ \dot{C_p}^o(t) \end{bmatrix} (1-H_\epsilon(\phi_\gamma(\vec{r}))) = \begin{bmatrix} -k_{ep}^i & k_{pe}^i \\ k_{ep}^i & -(k_{pe}^i+k_{elm}^i) \end{bmatrix} \begin{bmatrix} C_e^i(t) \\ C_p^i(t) \end{bmatrix} H_\epsilon(\phi_\gamma(\vec{r}))+ \begin{bmatrix} -k_{ep}^o & k_{pe}^o \\ k_{ep}^o & -(k_{pe}^o+k_{elm}^o) \end{bmatrix} \begin{bmatrix} C_e^o(t) \\ C_p^o(t) \end{bmatrix} (1-H_\epsilon(\phi_\gamma(\vec{r}))) \quad (20)$$

The time-discretized version for the above equation can thus be written as

$$\begin{bmatrix} C_e^i(j+1) \\ C_p^i(j+1) \\ C_e^o(j+1) \\ C_p^o(j+1) \end{bmatrix} = \begin{bmatrix} \tau_{11}^i & \tau_{12}^i & 0 & 0 \\ \tau_{21}^i & \tau_{22}^i & 0 & 0 \\ 0 & 0 & \tau_{11}^o & \tau_{12}^o \\ 0 & 0 & \tau_{21}^o & \tau_{22}^o \end{bmatrix} \begin{bmatrix} C_e^i(j) \\ C_p^i(j) \\ C_e^o(j) \\ C_p^o(j) \end{bmatrix} \quad (21)$$

where the relations between the interim kinetic parameters, the τ's and the pharmacokinetic parameters, the k's, arise from eq(3) and are given in the appendix.

This state (concentration) and parameter (pharmacokinetic as well as shape parameters) estimation problem can be solved using either stochastic estimation schemes such as EKF and its variants[9,10,22,57] or, deterministic schemes such as the Gauss-Newton (GN) filter.[39,58] In our work we propose an iteratively regularized deterministic GN-filter in a trust-region setting for our reconstructions. We define the state vector at time j as

$$\Theta_j \equiv \{\underbrace{C_e^i(j), C_p^i(j), C_e^o(j), C_p^o(j)}_{\boldsymbol{C}}, \underbrace{k_{pe}^i, k_{ep}^i, k_{elm}^i, k_{pe}^o, k_{ep}^o, k_{elm}^o}_{\boldsymbol{k}}, \underbrace{v_e^i, v_e^o, v_p^i, v_p^o}_{\boldsymbol{v}}, \underbrace{\alpha, \beta, \chi_1, \chi_2}_{\boldsymbol{\gamma}}\}. \quad (22)$$

Assuming our state equation is exact, we would need to explicitly reconstruct only Θ_0.

We can rewrite the state equation as

$$\begin{bmatrix} C_e^i(j+1) \\ C_p^i(j+1) \\ C_e^o(j+1) \\ C_p^o(j+1) \\ \boldsymbol{k} \\ \boldsymbol{v} \\ \boldsymbol{\gamma} \end{bmatrix} = \begin{bmatrix} \tau_{11}^i & \tau_{12}^i & 0 & 0 & 0 & 0 & 0 \\ \tau_{21}^i & \tau_{22}^i & 0 & 0 & 0 & 0 & 0 \\ 0 & 0 & \tau_{11}^o & \tau_{12}^o & 0 & 0 & 0 \\ 0 & 0 & \tau_{21}^o & \tau_{22}^o & 0 & 0 & 0 \\ 0 & 0 & 0 & 0 & I_6 & 0 & 0 \\ 0 & 0 & 0 & 0 & 0 & I_4 & 0 \\ 0 & 0 & 0 & 0 & 0 & 0 & I_{4m} \end{bmatrix} \begin{bmatrix} C_e^i(j) \\ C_p^i(j) \\ C_e^o(j) \\ C_p^o(j) \\ \boldsymbol{k} \\ \boldsymbol{v} \\ \boldsymbol{\gamma} \end{bmatrix} \quad (23)$$

where I_D denotes identity matrix of size $D \times D$ ($D \in \{6, 4, 4m\}$). The above equation can be written in simplified form as

$$\Theta_{j+1} = A(\Theta_j) \cdot \Theta_j = f(\Theta_j) \quad (24)$$

where f denotes the nonlinear state transition function, matrix $A(\Theta_j)$ is

$$A(\Theta_j) \equiv \begin{bmatrix} T^i & 0 & 0 \\ 0 & T^o & 0 \\ 0 & 0 & I_{4m+10} \end{bmatrix}; \qquad T^{i/o} = \begin{bmatrix} \tau_{11}^{i/o}(\mathbf{k}) & \tau_{12}^{i/o}(\mathbf{k}) \\ \tau_{21}^{i/o}(\mathbf{k}) & \tau_{22}^{i/o}(\mathbf{k}) \end{bmatrix} \tag{25}$$

The discrete-time measurement equation at time j can be formally written from (8) as

$$y_j \equiv g_j(\Theta_j) = g_j(f_{j-1}(\dots f_0(\Theta_0))) \tag{26}$$

3 Reconstruction scheme

3.1 Gauss-Newton filter scheme

The Gauss-Newton (GN) filter solves the state variable model with the state Eq. (23) and measurement equation (26) by solving the following regularized nonlinear least squares problem using the GN method:[39,58]

$$\hat{\Theta}_0 = \underset{\Theta_0}{\operatorname{argmin}}\, \mathcal{F}(\Theta_0) := \frac{1}{2} \left\| (\mathbf{g}(\Theta_0) - \mathbf{y}) \right\|^2 + \tau R(\Theta_0) \tag{27}$$

where τ is the regularization parameter and $R(\cdot)$ is the regularization functional, $\mathbf{y}$ and $\mathbf{g}(\Theta_0)$ are the concatenated set of observed and model-predicted measurements respectively.

$R(\Theta_0)$, the regularization functional is chosen here as a minimum-norm penalty:

$$R(\Theta_0) = \|\Theta_0 - \Theta_c\|^2 \tag{28}$$

where Θ_c represents an apriori known constant vector. The nonlinear least squares problem can be solved by iterative regularization scheme using either line search or trust region methodologies.[39,59,60] A regularized GN update p_Θ solves at the current iterate Θ:

$$\hat{p}_\Theta = \underset{p_\Theta}{\operatorname{argmin}} \left\| \begin{array}{c} \mathbf{J}(\Theta)p_\Theta + \mathbf{r} \\ \sqrt{\tau}(\Theta - \Theta_c + p_\Theta) \end{array} \right\|^2 \tag{29}$$

where the Jacobian $\mathbf{J}$ and the residual $\mathbf{r}$ are given by

$$\mathbf{J} = \begin{bmatrix} J_0 \\ \vdots \\ J_{M-1} \end{bmatrix}; \ \mathbf{r} = \begin{bmatrix} r_0 \\ \vdots \\ r_{M-1} \end{bmatrix}; \tag{30}$$

M denotes the number of time instants and Jacobian at time instant j is given by

$$J_{j-1} = G_{j-1}[\Theta_{j-1}]F_{j-1}[\Theta_{j-1}] \dots F_0[\Theta_0] \tag{31}$$

where $G[\cdot]$ and $F[\cdot]$ are the Frechet derivatives of measurement and state transition functions respectively. The residual at time instant j is given by

$$r_j = g_j(\Theta_j) - y_j = g_j(f_{j-1}(\dots f_0(\Theta_0))) - y_j; \tag{32}$$

3.2 Reconstruction algorithm

To solve the above minimization problem we propose a trust region based iteratively regularized Gauss-Newton filter algorithm. We first observe that for a linear residual, the Gauss-Newton

method converges in a single iteration. An iteratively (Tikhonov) regularized scheme needs to solve a succession of nonlinear regularized least squares sub-problems, each with different values of the regularization parameter, with the solution obtained for a given parameter used as the starting estimate for the next lower parameter-value.

Our computational experience shows that we need not solve each sub-problem exactly; hence assuming that a linear assumption to the residual is approximately valid, we shift to lower parameter values if we are close to a full Newton step for a "good" update,[32] with the "goodness" of the step being decided upon by the actual reduction in the residual with respect to its predicted decrease in our currently used trust region framework explained below.

Now, each step of a Gauss-Newton scheme needs to solve the problem 29, which is a least-squares version of the linear system $\mathbf{J_a} p_\Theta = -\mathbf{r_a}$, where we use the augmented Jacobian $\mathbf{J}_a \equiv \begin{bmatrix} \mathbf{J} \\ \sqrt{\tau} I \end{bmatrix}$ and the augmented residual $\mathbf{r}_a \equiv \begin{bmatrix} \mathbf{r} \\ \sqrt{\tau}(\Theta_0 - \Theta_c) \end{bmatrix}$.

The step p_Θ obtained from a Gauss-Newton step is found using either line-search or trust-region approaches in order that the overall algorithm exhibits global convergence. In our work, we choose to work with the trust region class of schemes, wherein we assume a quadratic model of the cost-function to locally hold in some ball (decided by a trust region radius) around the current estimate. The trust region's radius is varied with iteration as per the ratio of the actual to predicted cost-function-decreases.

Given a trust-region radius, the trust region step satisfies

$$\Delta = \|(\mathbf{J}_a^T \mathbf{J}_a + \lambda I)^{-1} \mathbf{J}_a^T \mathbf{r}_a\|_2 \tag{33}$$

where we calculate the parameter λ using a suitable root-finding technique.[60,61]

To ensure proper scaling, the variables are scaled as $\Theta = S \cdot \tilde{\Theta}$ using a diagonal scaling matrix S, with elements given by[59]

$$S_{ii} = \frac{1}{\sqrt{\sum_j J_{ij}^2 + \tau}} \tag{34}$$

Thus, from Eq. (33), we see that the scaled-domain counterparts of $\mathbf{J}_a$ and Δ, namely, $\tilde{\mathbf{J}}_a = \mathbf{J}_a \cdot S$ and $\tilde{\Delta}$ (the trust region radius in the scaled domain) respectively, satisfy

$$\tilde{\Delta} = \|(\tilde{\mathbf{J}}_a^T \tilde{\mathbf{J}}_a + \lambda I)^{-1} \tilde{\mathbf{J}}_a^T \mathbf{r}_a\|_2 \tag{35}$$

The update in the scaled domain $\tilde{p}_\Theta$ is then defined to satisfy the equation

$$\begin{bmatrix} \tilde{\mathbf{J}}_\mathbf{a} \\ \sqrt{\lambda} I \end{bmatrix} \tilde{p}_{\Theta_0} = - \begin{bmatrix} \mathbf{r}_\mathbf{a} \\ \mathbf{0} \end{bmatrix} \tag{36}$$

The update in the original domain p_Θ is thus given by

$$p_\Theta = S \tilde{p}_\Theta \tag{37}$$

We then calculate the cost function $\mathcal{F}$ and reduction ratio, $\rho = \frac{actual\ reduction}{predicted\ reduction}$ at the nominal estimate Θ^t. The regularization parameter, τ is reduced if ρ is above a threshold ρ_{th} with a minimum limit of τ_{min}. The trust region radius updating rule, values of η_1, η_2 and parameter γ_{bad} are based on the practical algorithm in Conn *et al.*[62] The algorithmic flow of reconstruction is shown in the algorithm table "Algorithm 1" below .

Algorithm 1 Trust region based iterative regularized Gauss-Newton filter

Initialization: Θ^0, $\Theta_c = \Theta^0$, Δ_0, $\eta_1 = 0.01$, $\eta_2 = 0.9$, $\tau_0 = 0.8$, $i = 0$
while $i < i_{max}$ **do**
    Calculate $\mathbf{J}^i$, $\mathbf{r}^i$, $\mathcal{F}(\Theta^i)$ using Θ^i
    calculate λ using (33)
    solve for p_Θ using (36) and (37)
    $\Theta^t = \Theta^i + p_\Theta$
    Evaluate $\mathcal{F}(\Theta^t)$ and ρ
    if $\rho > \eta_1$ **then**
        Accept update. $\Theta^{i+1} = \Theta^t$;
        if $\rho > \rho_{th}$ **then**
            $\tau_{i+1} = max(\tau_i/3, \tau_{min})$;
        end if
    else
        $\Theta^{i+1} = \Theta^i$;
    end if

    if $\rho > \eta_2$ **then**
        $\Delta_{i+1} = max(2.5 \cdot \|\tilde{p}_\Theta\|, \Delta_i)$;
    else if $\rho \geq \eta_1 \& \rho < \eta_2$ **then**
        $\Delta_{i+1} = \Delta_i$;
    else if $\rho \geq 0 \& \rho < \eta_1$ **then**
        $\Delta_{i+1} = 0.25 \cdot \|\tilde{p}_\Theta\|$;
    else if $\rho < 0$ **then**
        $\Delta_{i+1} = min(0.25 \cdot \|\tilde{p}_\Theta\|, max(0.0625, \gamma_{bad}) \cdot \Delta_i)$;
    end if

    $i = i + 1$;
end while
Choose the stopping iterate when $\epsilon_{rel} < tol$, or, the data-residual staying stable or toggling across iterations.

The following relative measure[39] of the residual is used as a reflection of "how much" of the residual is left in the range of the augmented Jacobian and serves as a useful stopping criterion.

$$\epsilon_{rel} = \frac{\|\mathcal{P}_{\mathbf{J}_a}\mathbf{r}_a\|}{\|\mathbf{r}_a\|} \tag{38}$$

where $\mathcal{P}_{\mathbf{J}_a}$ is the orthogonal projection onto the range space of $\mathbf{J}_a$.

3.3 Frechet derivative calculation

3.3.1 Frechet derivative of measurement function

The Frechet derivative of the measurement function (eq (8)) with respect to the parameter set at a given time instant j is given by

$$G_j = \left[\underbrace{\frac{\partial y_j}{\partial \mathcal{C}(j)}}_{D\times 4} \quad \underbrace{\frac{\partial y_j}{\partial k}}_{D\times 6} \quad \underbrace{\frac{\partial y_j}{\partial v}}_{D\times 4} \quad \underbrace{\frac{\partial y_j}{\partial \gamma}}_{D\times 4m} \right] \tag{39}$$

The sensitivity equation with respect to $s \in \{C_e^i(j), C_p^i(j), C_e^o(j), C_p^o(j),$ $k_{pe}^i, k_{ep}^i, k_{elm}^i, k_{pe}^o, k_{ep}^o, k_{elm}^o, v_e^i, v_e^o, v_p^i, v_p^o, \alpha, \beta, \chi_1, \chi_2\}$ is calculated using the chain rule as:

$$\frac{\partial y_j(\vec{r}_d)}{\partial s} = \frac{1}{\Phi_m(\vec{r}_d, j)} \left[\frac{\partial \Phi_m(\vec{r}_d, j)}{\partial \mu_{axf}(j)} \times \frac{\partial \mu_{axf}(j)}{\partial s} + \frac{\partial \Phi_m(\vec{r}_d, j)}{\partial \mu_{amf}(j)} \times \frac{\partial \mu_{amf}(j)}{\partial s} \right] \tag{40}$$

The derivative of the fluence Φ_m with respect to μ_{axf} is given in Fedele *et al.*[54] To derive the sensitivity of μ_{axf} and μ_{amf} with respect to unknowns Θ, consider equation (19) for the time-

varying absorption coefficient

$$\mu(\vec{r},j) = ln10 \cdot \epsilon \cdot [(C_e^i(j)v_e^i + C_p^i(j)v_p^i)H_\epsilon(\phi(\vec{r})) + (C_e^o(j)v_e^o + C_p^o(j)v_p^o)(1 - H_\epsilon(\phi(\vec{r})))] \quad (41)$$

The sensitivity of $\mu(\vec{r},j)$ with respect to $\{C_e^i(j), C_p^i(j), C_e^o(j), C_p^o(j),\ v_e^i, v_e^o, v_p^i, v_p^o\}$ are given below

$$\frac{\partial \mu(\vec{r},j)}{\partial C_{e/p}^i(j)} = ln10 \cdot \epsilon \cdot v_{e/p}^i H_\epsilon(\phi_\gamma(\vec{r})); \qquad \frac{\partial \mu(\vec{r},j)}{\partial v_{e/p}^i} = ln10 \cdot \epsilon \cdot C_{e/p}^i(j) H_\epsilon(\phi_\gamma(\vec{r})); \quad (42)$$

$$\frac{\partial \mu(\vec{r},j)}{\partial C_{e/p}^o(j)} = ln10 \cdot \epsilon \cdot v_{e/p}^o (1 - H_\epsilon(\phi_\gamma(\vec{r}))); \qquad \frac{\partial \mu(\vec{r},j)}{\partial v_{e/p}^o} = ln10 \cdot \epsilon \cdot C_{e/p}^o(j)(1 - H_\epsilon(\phi_\gamma(\vec{r}))); \quad (43)$$

The variation of $\mu(\vec{r},j)$ with respect to $\boldsymbol{\gamma} \in \{\boldsymbol{\alpha}, \boldsymbol{\zeta}, \boldsymbol{\chi}\}$ is given by

$$\frac{\partial \mu(\vec{r},j)}{\partial \gamma} = \frac{\partial \mu(\vec{r},j)}{\partial C_e(\vec{r},j)} \frac{\partial C_e(\vec{r},j)}{\partial \gamma} + \frac{\partial \mu(\vec{r},j)}{\partial C_p(\vec{r},j)} \frac{\partial C_p(\vec{r},j)}{\partial \gamma} + \frac{\partial \mu(\vec{r},j)}{\partial v_e(\vec{r})} \frac{\partial v_e(\vec{r})}{\partial \gamma} + \frac{\partial \mu(\vec{r},j)}{\partial v_p(\vec{r})} \frac{\partial v_p(\vec{r})}{\partial \gamma} \quad (44)$$

where (from (19))

$$\frac{\partial \mu(\vec{r},j)}{\partial C_{e/p}(\vec{r},j)} = ln10 \cdot \epsilon \cdot v_{e/p}(\vec{r}); \qquad \frac{\partial \mu(\vec{r},j)}{\partial v_{e/p}(\vec{r})} = ln10 \cdot \epsilon \cdot C_{e/p}(\vec{r},j); \quad (45)$$

Further, from the level-set representation of $C_{e/p}$ (17) and $v_{e/p}$ (18), we have

$$\frac{\partial C_{e/p}(\vec{r},j)}{\partial \gamma} = (C^i_{e/p}(j) - C^o_{e/p}(j))H'_\epsilon(\phi_\gamma(\vec{r}))\frac{\partial \phi}{\partial \gamma}; \qquad \frac{\partial v_{e/p}(\vec{r})}{\partial \gamma} = (v^i_{e/p} - v^o_{e/p})H'_\epsilon(\phi_\gamma(\vec{r}))\frac{\partial \phi}{\partial \gamma}; \tag{46}$$

where the sensitivities of the level-set, ϕ with repect to the shape parameters are given by[37]

$$\frac{\partial \phi}{\partial \alpha_l} = \psi(\|\zeta_j(\mathbf{x} - \chi_j)\|^\dagger) \tag{47}$$

$$\frac{\partial \phi}{\partial \zeta_l} = \alpha_j \zeta_l \frac{\|(\mathbf{x} - \chi_l)\|^2}{\|\zeta_l(\mathbf{x} - \chi_l)\|^\dagger}\psi'(\|\zeta_j(\mathbf{x} - \chi_l)\|^\dagger) \tag{48}$$

$$\frac{\partial \phi}{\partial \chi^k_l} = -\alpha_l \zeta_l^2 \frac{(x^k - \chi^k_l)}{\|\zeta_l(\mathbf{x} - \chi_l)\|^\dagger}\psi'(\|\zeta_l(\mathbf{x} - \chi_l)\|^\dagger) \tag{49}$$

where χ^k_l is the kth component of center χ_l.

3.3.2 Frechet derivative of state transition function

The state transition equation is given by

$$\begin{bmatrix} C_e^i(j+1) \\ C_p^i(j+1) \\ C_e^o(j+1) \\ C_p^o(j+1) \\ \boldsymbol{k}(j+1) \\ \boldsymbol{v}(j+1) \\ \boldsymbol{\alpha}(j+1) \\ \boldsymbol{\zeta}(j+1) \\ \boldsymbol{\chi}(j+1) \end{bmatrix} = \begin{bmatrix} b_1^i(\boldsymbol{k},j) \\ b_2^i(\boldsymbol{k},j) \\ b_1^o(\boldsymbol{k},j) \\ b_2^o(\boldsymbol{k},j) \\ \boldsymbol{k}(j) \\ \boldsymbol{v}(j) \\ \boldsymbol{\alpha}(j) \\ \boldsymbol{\zeta}(j) \\ \boldsymbol{\chi}(j) \end{bmatrix} \tag{50}$$

where

$$\begin{aligned} b_1^i(\boldsymbol{k},j) &\equiv \tau_{11}^i(\boldsymbol{k})C_e^i(j) + \tau_{12}^i(\boldsymbol{k})C_p^i(j) \\ b_2^i(\boldsymbol{k},j) &\equiv \tau_{21}^i(\boldsymbol{k})C_e^i(j) + \tau_{22}^i(\boldsymbol{k})C_p^i(j) \\ b_1^o(\boldsymbol{k},j) &\equiv \tau_{11}^o(\boldsymbol{k})C_e^o(j) + \tau_{12}^o(\boldsymbol{k})C_p^o(j) \\ b_2^o(\boldsymbol{k},j) &\equiv \tau_{21}^o(\boldsymbol{k})C_e^o(j) + \tau_{22}^o(\boldsymbol{k})C_p^o(j) \end{aligned} \tag{51}$$

The variables $\tau_{pq}^{i/o}$ $(p,q=1,2)$ are functions of parameters $\{k_{ep}^{i/o}, k_{pe}^{i/o}, k_{elm}^{i/o}\}$ whose expressions are given in the appendix. The Frechet derivative, F_j of the state transition function at time instant j is given by

$$F_j = \begin{bmatrix} \tau_{11}^i & \tau_{21}^i & 0 & 0 & \frac{\partial b_1^i}{\partial k_{pe}^i} & \frac{\partial b_1^i}{\partial k_{ep}^i} & \frac{\partial b_1^i}{\partial k_{elm}^i} & 0 & 0 & 0 & \mathbf{0} \\ \tau_{21}^i & \tau_{22}^i & 0 & 0 & \frac{\partial b_2^i}{\partial k_{pe}^i} & \frac{\partial b_2^i}{\partial k_{ep}^i} & \frac{\partial b_2^i}{\partial k_{elm}^i} & 0 & 0 & 0 & \mathbf{0} \\ 0 & 0 & \tau_{11}^o & \tau_{21}^o & 0 & 0 & 0 & \frac{\partial b_1^o}{\partial k_{pe}^o} & \frac{\partial b_1^o}{\partial k_{ep}^o} & \frac{\partial b_1^o}{\partial k_{elm}^o} & \mathbf{0} \\ 0 & 0 & \tau_{21}^o & \tau_{22}^o & 0 & 0 & 0 & \frac{\partial b_2^o}{\partial k_{pe}^o} & \frac{\partial b_2^o}{\partial k_{ep}^o} & \frac{\partial b_2^o}{\partial k_{elm}^o} & \mathbf{0} \\ \mathbf{0} & \mathbf{0} & \mathbf{0} & \mathbf{0} & \mathbf{0} & \mathbf{0} & \mathbf{0} & \mathbf{0} & \mathbf{0} & \mathbf{0} & \mathbf{I}_{4m+10} \end{bmatrix}$$

4 Numerical Studies

4.1 Test-case and reconstruction settings

A computational domain of size $4 \times 4\ cm$, with origin as the center is considered for our numerical test cases.[63] Eight detectors are placed symmetrically on each of the 4 sides of the domain, as shown in the figure 2. Four collimated sources each with strength 10mW modulated at 100MHz are placed at the center of each side and modelled at the depth of one mean free path as in Schweiger *et al.*[64] The homogeneous optical properties of the tissue-mimicking phantom used in FOT with ICG as a fluorophore (at excitation and emission wavelengths $785\ nm$ and $830\ nm$ respectively) are given by:[65] $\mu_{axi} = 0.031\ cm^{-1}$, $\mu_{ami} = 0.00415\ cm^{-1}$, $\mu'_{sx} = 10.95\ cm^{-1}$, $\mu'_{sm} = 9.29\ cm^{-1}$, $\tau = 0.56\ ns$, $\phi = 0.016$, $R_{x,m} = 0.431$, $\epsilon_x = 130000\ M^{-1}cm^{-1}$, $\epsilon_m = 11000\ M^{-1}cm^{-1}$.

The pharmacokinetic rates mentioned for invasive ductal carcinoma (IDC) and adenocarcinoma (AC)[21] are used to obtain synthetic measurement data. We assume 6.5 μM concentration of fluorophore is injected[43] via bolus. At the first time instant in the data generation, we assume the fluorophore concentration in the plasma compartment to be 6.5 μM and 0 μM in the EES

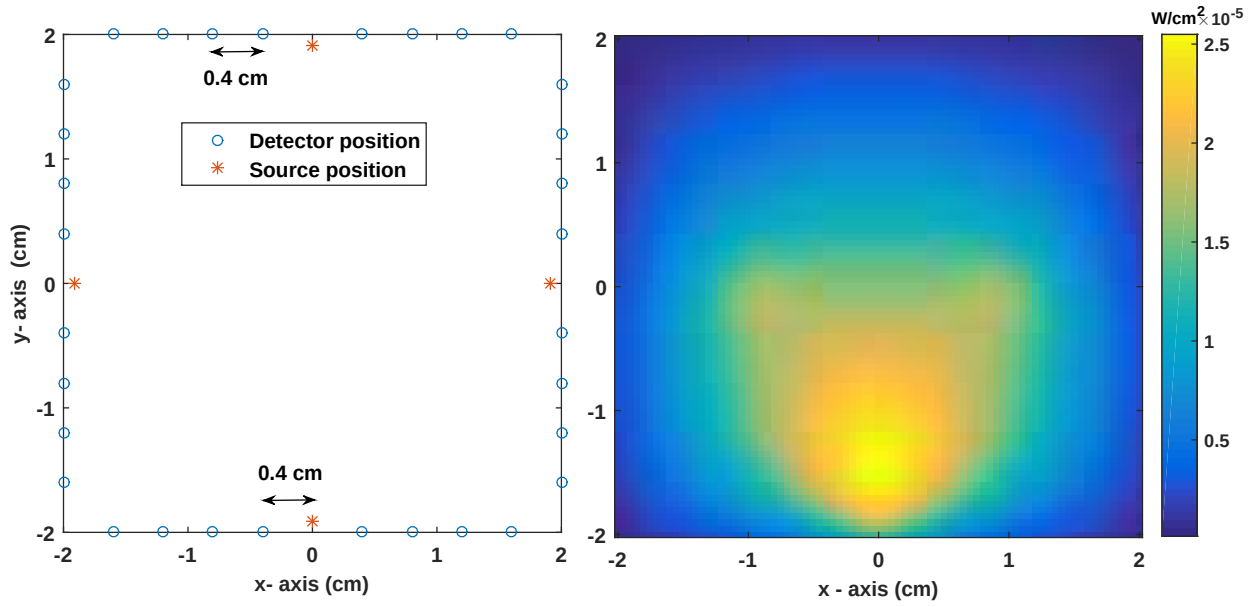

Fig 2 Schematic on the left represents source and detector setting for the numerical study; Figure on the right is a typical fluence map obtained for the two object phantom for the IDC case (parameters in table 2) with source on bottom face (at (0,-2))

compartment. Measurements are taken for 40 time instants with a sampling interval of 5 sec. At each time instant one source is on and measurements are taken from all the detectors (32 in our setting). Measurements used for reconstruction are the complex log intensity[59] of the fluence at the emission wavelength for all time instants (1280 in this setting).

The data are generated using a finer mesh discretized with 160801 nodes containing 320000 triangular elements. Reconstructions are performed using a coarser mesh discretized with 6561 nodes containing 12800 triangular elements. Frechet derivatives evaluated using the method of adjoints is validated using finite difference method.

Numerical studies are done for each of the two cancer-types (IDC and AC), for two phantoms; "T" denoting a two-object phantom (adjacently-placed "smoothed corner square like" objects) with each having approximate extent of $0.5cm$ in each direction with their boundaries separated by approximately $1.5cm$, and, "B" being a single bean shaped phantom with lateral and longitudinal

Table 1 SNR of the synthetic data

T Phantom(IDC)	SNR(dB)	B Phantom (IDC)	SNR(dB)
I-T1	38.99	I-B1	39.35
I-T2	33.2	I-B2	33.47
I-T3	29.77	I-B3	29.75
T Phantom (AC)	SNR(dB)	B Phantom (AC)	SNR(dB)
A-T1	39.02	A-B1	39.29
A-T2	32.87	A-B2	33.4
A-T3	29.35	A-B3	29.83

extents being approximately $0.7cm$ and $1.3cm$ respectively. Data is generated for the two phantoms at three SNR levels as given in table 1. All the computations are performed in the Matlab ® 2016a programming environment.

Initial estimates for pharmacokinetic rates are taken in between healthy and tumor values. Initial fluorophore concentration in plasma compartment (C_p^i and C_p^o) assumed to be 6.5 μM and concentration of the fluorophore in EES compartment (C_e^i and C_e^o) is assumed to be 0 μM. The algorithm is terminated when $\epsilon_{rel} < tol$, or, the data-residual staying stable or toggling across iterations.

The shape reconstructions of two-object and bean phantoms for IDC as well as AC under various noise conditions, are shown in figures 3 and 4 respectively. The concentration curves (with respect to time) for both phantoms corresponding to regions inside and outside the tumor in IDC and AC settings are shown respectively in figures (5 for two-object phantom, 6 for bean phantom) and (7 for two-object phantom, 8 for bean phantom). In the figures, a time-index is defined as representing the sampling interval used (5 seconds in our case).

Tables 2 and 3 show the reconstructed values of the pharmacokinetic parameters for IDC and AC tumor cases respectively. In order to gauge the performance of the algorithm, across all test cases considered, (i.e along each row) we evaluate across all cases for each parameter, (a) the normalized mean square error (Row NMSE) of the reconstructions, and, (b) the maximal normalized

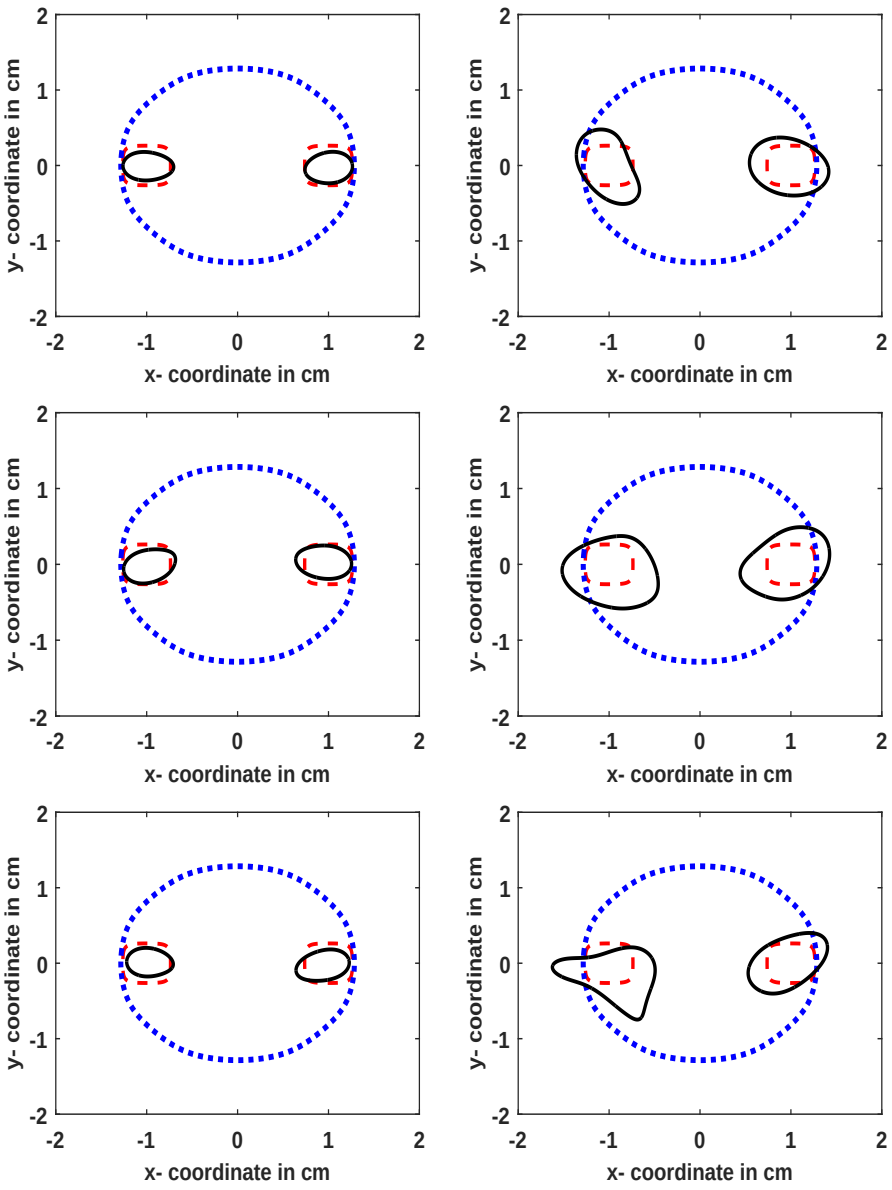

Fig 3 Reconstruction of two object phantom for IDC (left column; top-to-down: data-sets I-T1, I-T2, I-T3) and AC (right column; top-to-down: data-sets A-T1, A-T2, A-T3) tumor cases. Blue dotted line denotes the initial level-set, red dashed line denotes the shape of true object, and black solid line denotes the reconstructed shape.

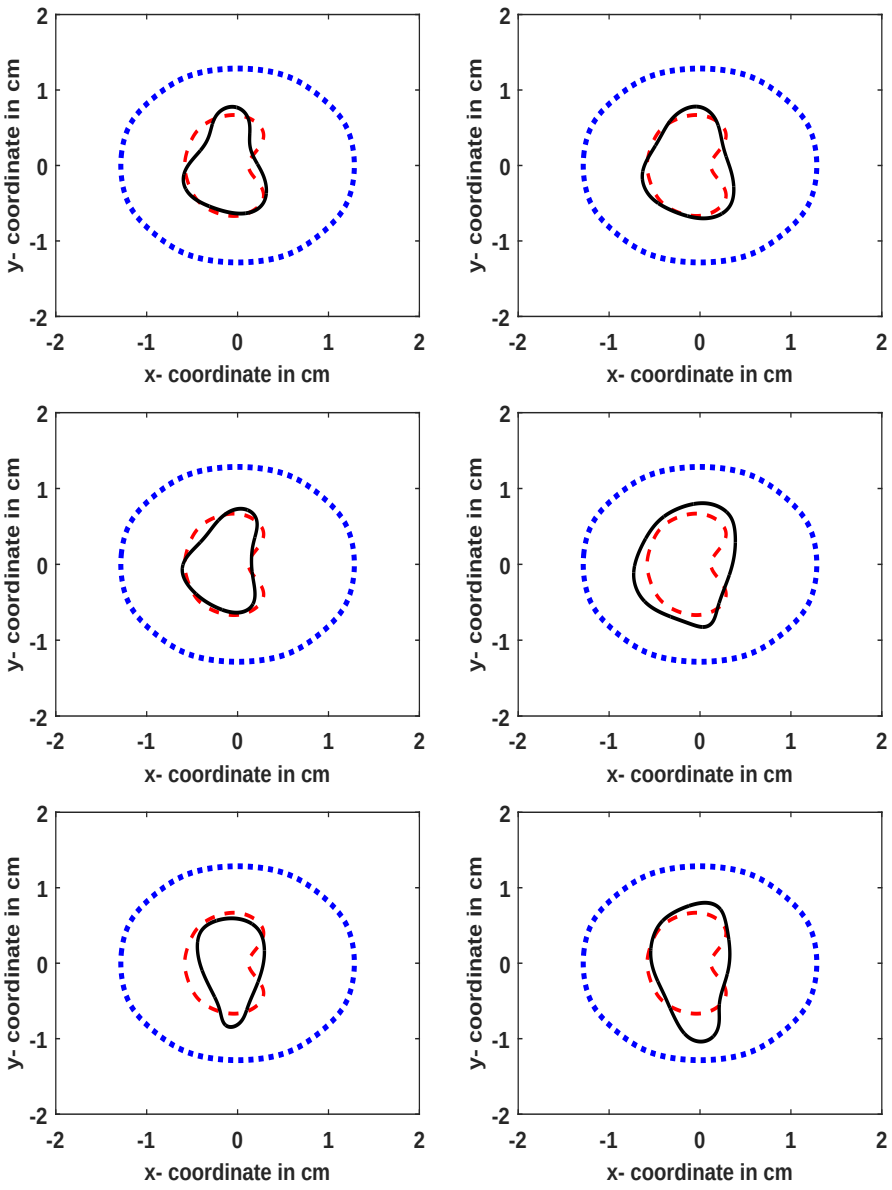

Fig 4 Reconstruction of bean shape phantom for IDC (left column; top-to-down: data-sets I-B1, I-B2, I-B3) and AC (right column; top-to-down: data-sets A-B1, A-B2, A-B3) tumor cases. Blue dotted line denotes the initial level-set, red dashed line denotes the shape of true object, and black solid line denotes the reconstructed shape.

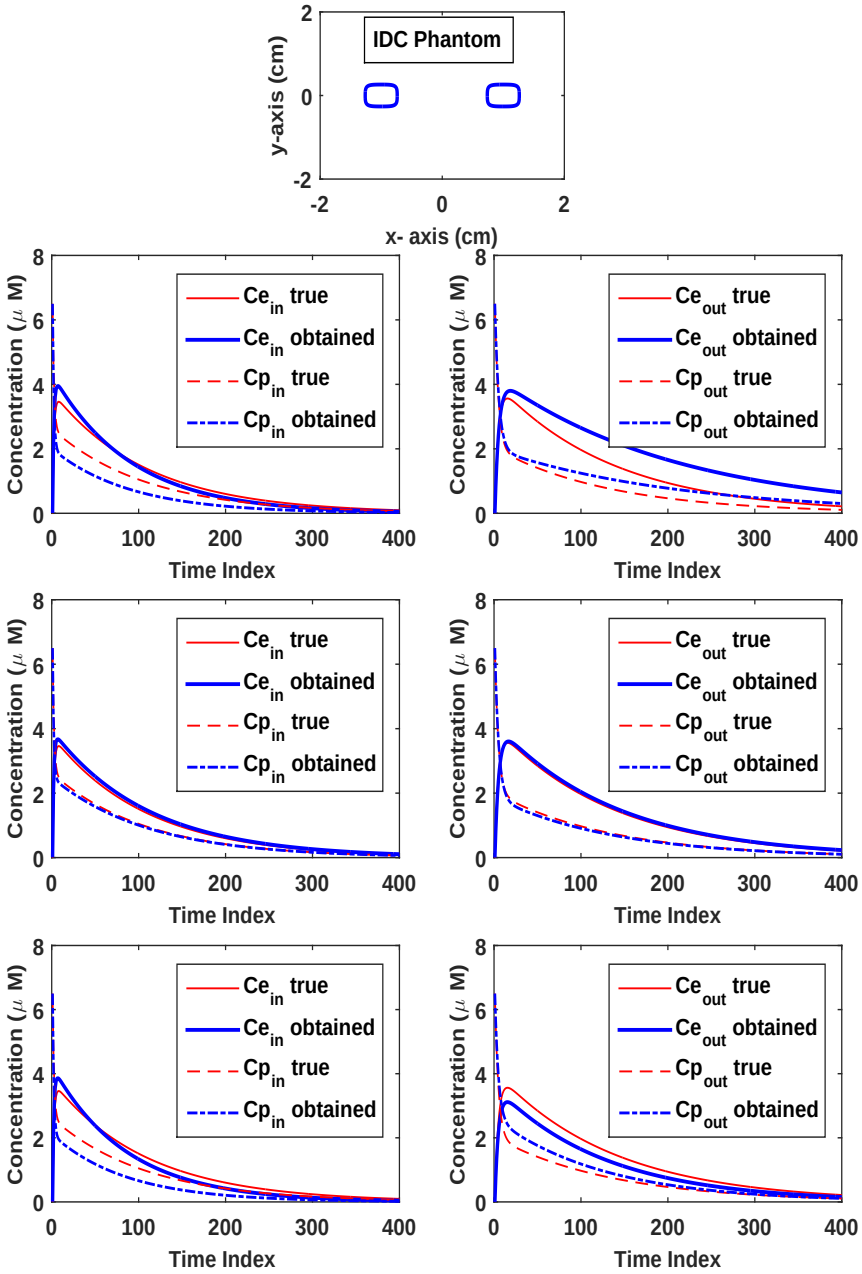

Fig 5 Concentration vs time plot for two object phantom for IDC tumor; 1 time-index= 5 seconds. Schematic of phantom placed on top. Red denotes the decay of concentration in true phantom and blue denotes the decay in reconstructed phantom. Left column shows Ce_{in} and Cp_{in} plots in the tumor region. Right column shows Ce_{out} and Cp_{out} plots outside the tumor region. First row corresponds to dataset I-T1, second row to dataset I-T2, and third row to dataset I-T3

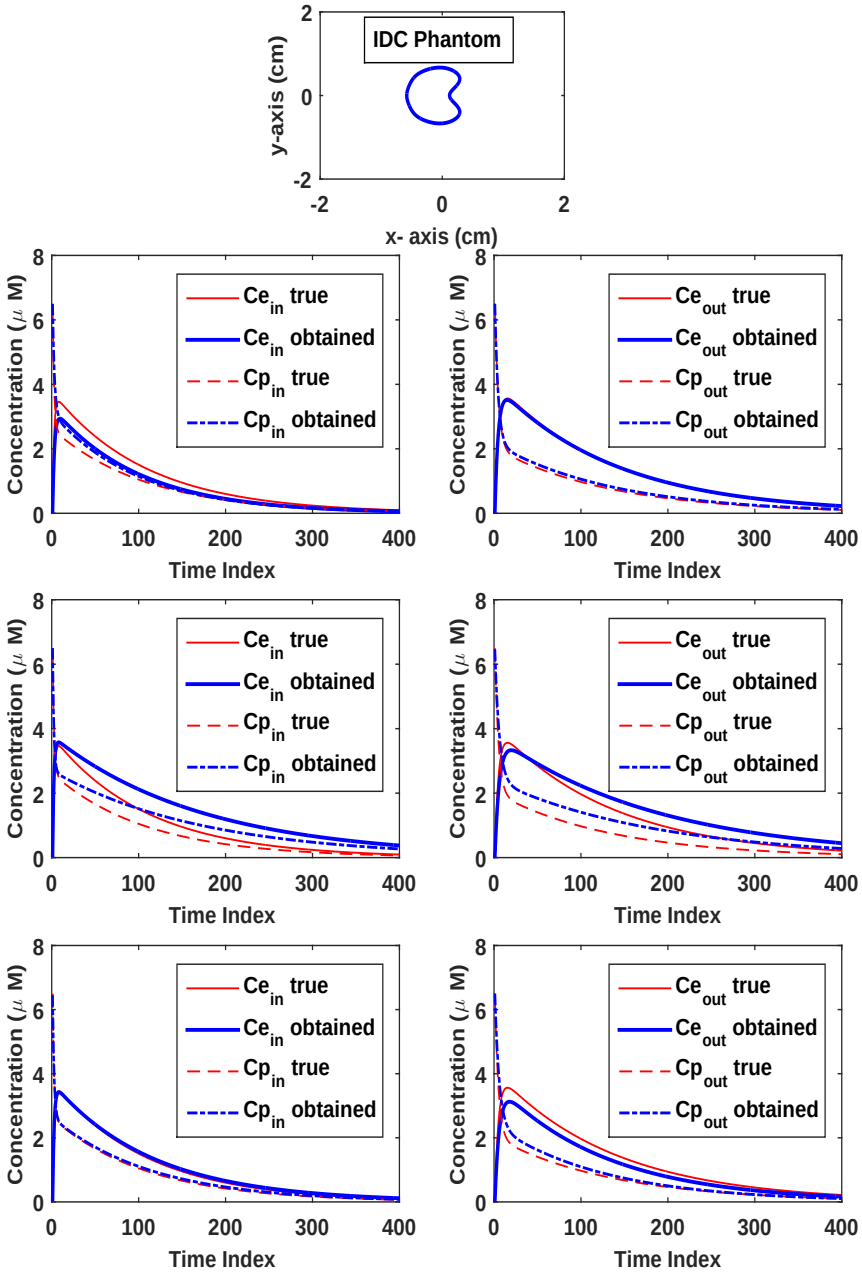

Fig 6 Concentration vs time plot for bean shape object phantom for IDC tumor; 1 time-index= 5 seconds. Schematic of phantom placed on top. Red denotes the decay of concentration in true phantom and blue denotes the decay in reconstructed phantom. Left column shows Ce_{in} and Cp_{in} plots in the tumor region. Right column shows Ce_{out} and Cp_{out} plots outside the tumor region. First row corresponds to dataset I-B1, second row to dataset I-B2, and third row to dataset I-B3

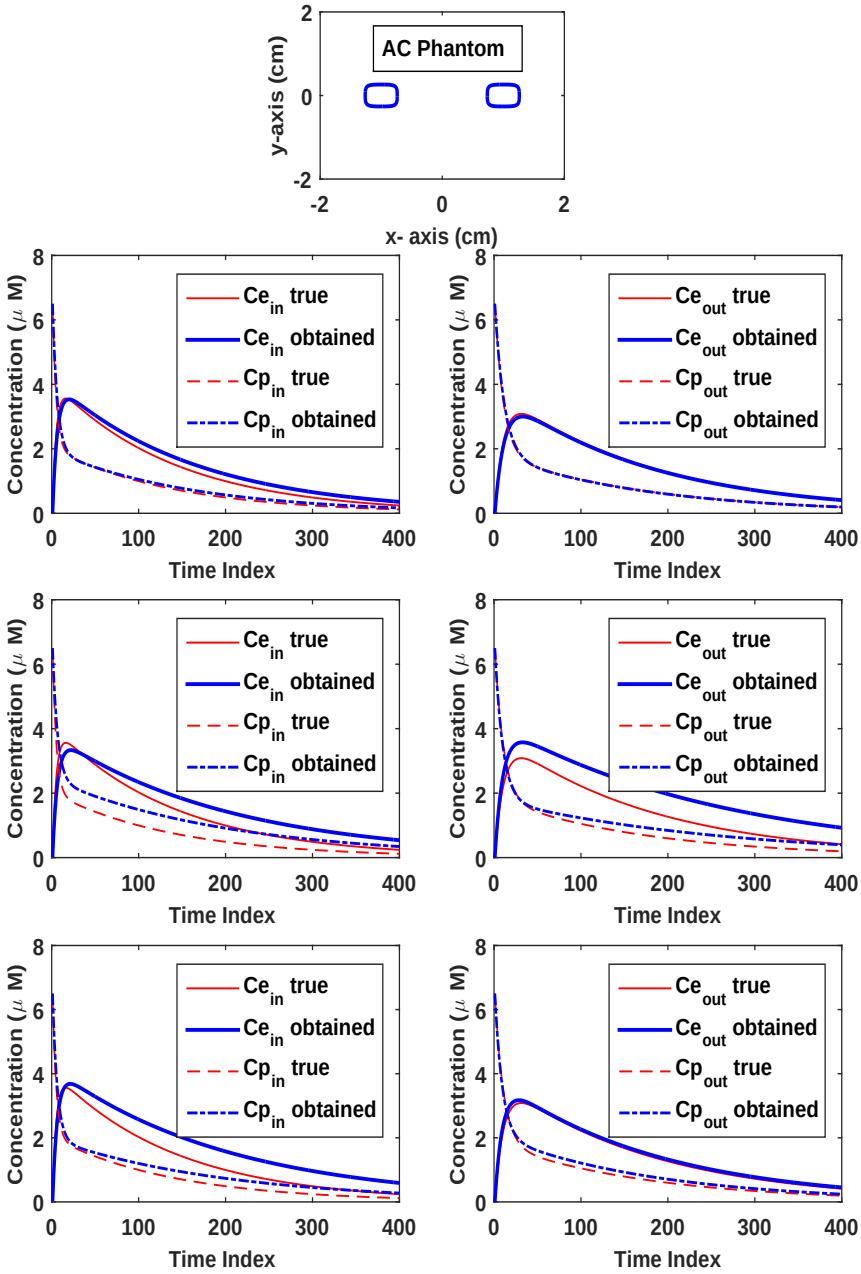

Fig 7 Concentration vs time plot for two object phantom for AC tumor; 1 time-index= 5 seconds. Schematic of phantom placed on top. Red denotes the decay of concentration in true phantom and blue denotes the decay in reconstructed phantom. Left column shows Ce_{in} and Cp_{in} plots in the tumor region. Right column shows Ce_{out} and Cp_{out} plots outside the tumor region. First row corresponds to dataset A-T1, second row to dataset A-T2, and third row to dataset A-T3

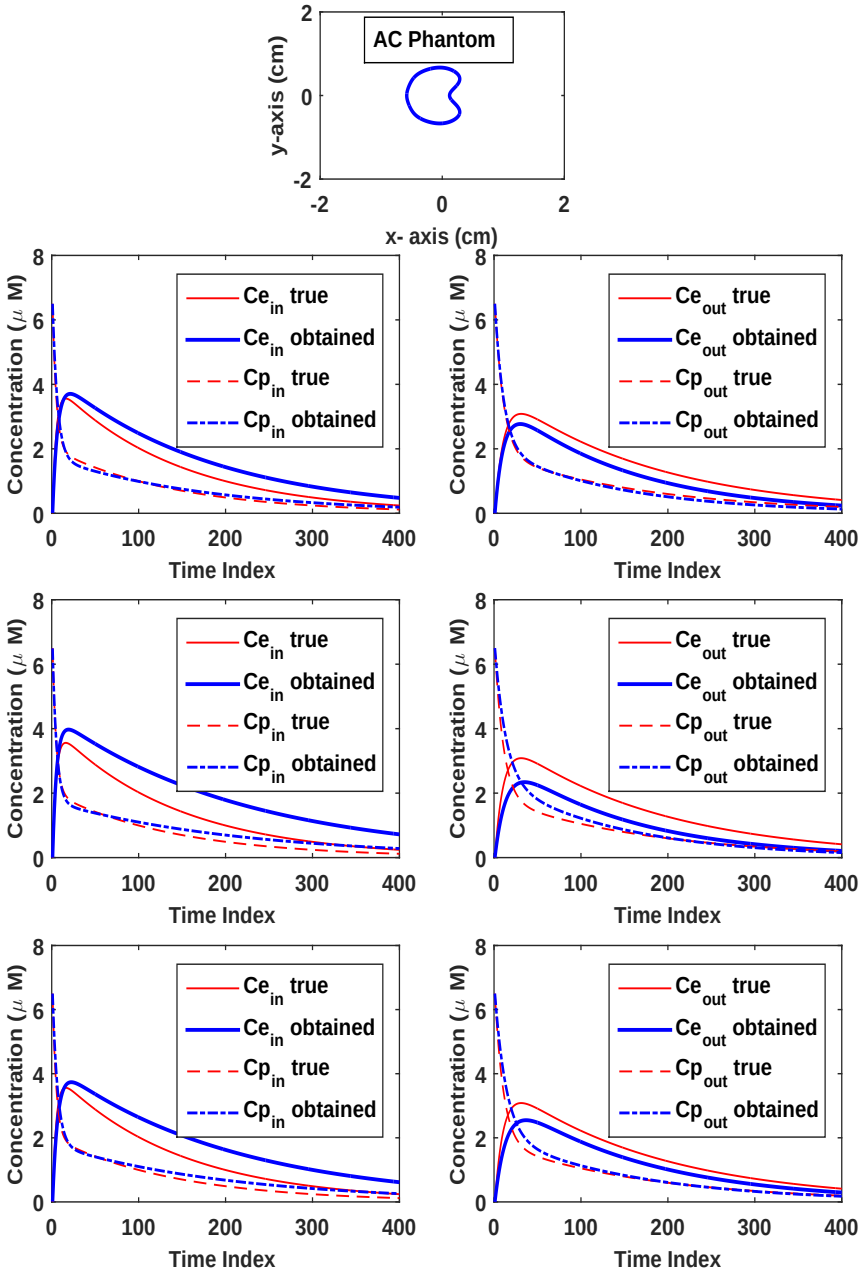

Fig 8 Concentration vs time plot for bean shape object phantom for AC tumor; 1 time-index= 5 seconds. Schematic of phantom placed on top. Red denotes the decay of concentration in true phantom and blue denotes the decay in reconstructed phantom. Left column shows Ce_{in} and Cp_{in} plots in the tumor region. Right column shows Ce_{out} and Cp_{out} plots outside the tumor region. First row corresponds to dataset A-B1, second row to dataset A-B2, and third row to dataset A-B3

error (MNE) in the reconstruction. The evaluations in (a) and (b) above are found in the last two columns respectively of the tables 2 and 3.

The contrast in the pharmacokinetic-rates and plasma-volume fractions indicate the presence of high-permeability and angiogenesis respectively in the tumor region. From our reconstructions we see that we are able to obtain a good delineation between tumor and healthy tissue as well as the contrast in the pharmacokinetic rates and plasma-volume fraction. We observe that the reconstructions are reasonably stable for data sets of SNR about 30dB, below which the quality and stability of reconstructions tend to go down.

Table 2 Pharmacokinetic parameters for invasive ductal carcinoma (IDC) test cases with average and maximal errors; a "*" in the last two columns would indicate that the error is not normalized owing to true values being zero

		Reconstructed values							
Parameter	True	I-T1	I-T2	I-T3	I-B1	I-B2	I-B3	Row NMSE	MNE
C_e^i	0	0.01	0.01	0.01	6×10^{-4}	0.01	0.01	*8 $\times10^{-5}$	*0.01
C_e^o	0	0	0.0029	0	0	0	0	*1 $\times10^{-6}$	*0.0029
C_p^i	6.5	6.49	6.5	6.5	6.49	6.5	6.45	8 $\times10^{-6}$	0.0073
C_p^o	6.5	6.5	6.5	6.5	6.5	6.46	6.5	5 $\times10^{-6}$	0.0059
k_{pe}^i	0.0687	0.0896	0.0900	0.0900	0.0453	0.0803	0.0659	0.07	0.34
k_{pe}^o	0.0306	0.0282	0.0282	0.0265	0.0315	0.0225	0.0220	0.03	0.28
k_{ep}^i	0.0496	0.0436	0.0583	0.0470	0.0446	0.0586	0.0484	0.01	0.18
k_{ep}^o	0.0166	0.0142	0.0140	0.0206	0.0185	0.0153	0.0157	0.02	0.24
k_{elm}^i	0.00449	0.0070	0.0047	0.0070	0.0041	0.0028	0.0042	0.13	0.55
k_{elm}^o	0.00446	0.0029	0.0047	0.0038	0.0041	0.0028	0.0040	0.05	0.38
v_e^i	0.3	0.4423	0.4390	0.4770	0.3556	0.3144	0.3385	0.14	0.58
v_e^o	0	0	3.1×10^{-6}	0	0	0	0	*1.5×10^{-12}	*3.1×10^{-6}
v_p^i	0.0600	0.0700	0.0498	0.0700	0.0669	0.0700	0.0700	0.02	0.16
v_p^o	0.0200	0.0190	0.0200	0.0160	0.0198	0.0167	0.0175	0.01	0.19

Table 3 Pharmacokinetic parameters for Adenocarcinoma (AC) test cases with average and maximal errors; a "*" in the last two columns would indicate that the error is not normalized owing to true values being zero

		Reconstructed values							
Parameter	True	A-T1	A-T2	A-T3	A-B1	A-B2	A-B3	Row NMSE	MNE
C_e^i	0	0.01	0.01	0.01	0.01	0.0017	0	*8.37×10^{-5}	*0.01
C_e^o	0	0	0	0	0	0	0	*0	*0
C_p^i	6.5	6.5	6.5	6.5	6.5	6.49	6.5	2×10^{-7}	1.3×10^{-3}
C_p^o	6.5	6.5	6.5	6.5	6.49	6.5	6.5	1×10^{-10}	3×10^{-5}
k_{pe}^i	0.0292	0.0225	0.0199	0.0229	0.0223	0.0286	0.0216	0.05	0.31
k_{pe}^o	0.0114	0.0103	0.0136	0.0133	0.0102	0.0071	0.0075	0.05	0.37
k_{ep}^i	0.0158	0.0118	0.0136	0.0117	0.0100	0.0121	0.0100	0.08	0.36
k_{ep}^o	0.0065	0.0060	0.0066	0.0082	0.0069	0.0067	0.0057	0.02	0.26
k_{elm}^i	0.0043	0.0038	0.0025	0.0031	0.0039	0.0032	0.0033	0.06	0.41
k_{elm}^o	0.0035	0.0035	0.0025	0.0031	0.0039	0.0032	0.0033	0.02	0.28
v_e^i	0.2000	0.0794	0.0645	0.0891	0.1317	0.0901	0.0967	0.3	0.67
v_e^o	0	0	0	0	0	0	0	*0	*0
v_p^i	0.0400	0.0472	0.0291	0.0342	0.0428	0.0416	0.0377	0.02	0.27
v_p^o	0.0200	0.0191	0.0199	0.0187	0.0196	0.0170	0.0185	0.01	0.15

4.2 Quantification of errors

To quantify the quality of our shape based reconstructions we use four error measures, namely, normalized error of area-parameter product across time instants, the distance of the centroid of the reconstructed object from the actual object, the Dice coefficient for the shape reconstructions, and normalized mean square error (NMSE) for the pharmacokinetic rates.

In addition, we also use an NMSE for pointwise evaluated pharmacokinetic rate and volume fraction images in order to get an image-quality metric for our shape-based reconstructions. We mapped our shape and pharmacokinetic parameter reconstructions into pointwise values to compute these NMSEs. The spatial values are obtained using equation 11.

The area-parameter product error measure,[38] E_{AP} is defined across all the time instants at which measurements are taken as

$$E_{AP} = \left(\left[\frac{\sum_{j=1}^{M} |\mu_{rec}^{i}(j) A_{rec} - \mu_{ac}^{i}(j) A_{ac}|}{\sum_{j=1}^{M} |\mu_{ac}^{i}(j) A_{ac}|} \right] / M \right) \times 100\%; \tag{52}$$

where A_{ac}, A_{rec} represents the area of actual and reconstructed object respectively, $\mu_{rec}^{i}(j)$ (respectively $\mu_{ac}^{i}(j)$) represents reconstructed (respectively actual) fluorophore absorption coefficient (41) inside tumor region at time instant j. This definition allows emphasis w.r.t. time instants with more significant product values.

Area of an object is given by

$$A_{object} = a_{element} \sum_{i,j} \chi_{object}(x_i, y_j) \tag{53}$$

where $a_{element}$ is the area of an element (a constant in our studies), $\chi_{object}(\cdot)$ is the characteristic function with respect to object support, (i, j) represents the indices of centroid coordinates x and y of the discretized domain. The centroid coordinates of an object is given by

$$\bar{x}_{object} = \frac{\sum_{i,j} x_i \chi_{object}(x_i, y_j)}{A_{object}}; \; \bar{y}_{object} = \frac{\sum_{i,j} y_j \chi_{object}(x_i, y_j)}{A_{object}} \tag{54}$$

The Euclidean distance between the centroids of reconstructed object and actual object is given by

$$E_c = \sqrt{(\bar{x}_{rec} - \bar{x}_{ac})^2 + (\bar{y}_{rec} - \bar{y}_{ac})^2} \tag{55}$$

The Dice coefficient[66] quantifies the localization and similarity of the shape reconstruction with the original shape. If S denotes the set of nodes inside the reconstructed object and H denotes the

set of nodes inside the true object, the Dice coefficient is given by

$$D(S,H) = \frac{2|S \cap H|}{|S| + |H|} \tag{56}$$

$|S \cap H|$ denotes the number of nodes present in S and also belongs to H. The Dice coefficient varies from 0 (indicating complete mismatch) to 1 (indicating accurate shape reconstruction).

The NMSE defined for a reconstructed quantity $\boldsymbol{X^r}$ with respect to its actual value $\boldsymbol{X^a}$ is defined as

$$E_{NMSE} = \frac{\|\boldsymbol{X^r} - \boldsymbol{X^a}\|^2}{\|\boldsymbol{X^a}\|^2} \tag{57}$$

The error metrics for the reconstruction of two phantoms at different noise levels are tabulated in table 4. We note that the NMSE for the pharmacokinetic rates evaluated in this table is based on the reconstructions of the concatenated vector $\boldsymbol{k}$ as shown in eq(22).

The error metrics evaluated further emphasize the good localization in general given by our approach for the small (near/sub-cm) phantoms in our study, in addition to a reasonable error in the reconstructed pharmacokinetic parameters and the area-parameter-product aspect.

In the table 5, in order to relate our shape-based results to pointwise error estimates with the purpose of checking image-quality acceptability with respect to existing literature (to the best of our knowledge, the only paper that solves for the present pharmacokinetic parameters along with volume fractions in a "one-step" reconstruction considering a fully-nonlinear FOT model is the work of Alacam *et al.*;[9] they solve the pointwise problem with an extended Kalman filter), we

Table 4 Error measures for the shape reconstructions (for the two object case the centroid error is an ordered pair (a,b) corresponding to each object)

Phantom	$E_{AP}\%$	$E_C(cm)$	$D(S,H)$	$E_{NMSE}(\boldsymbol{k})$
I-T1	1.29	(0.04, 0.04)	0.84	0.058
I-T2	2	(0.14, 0.07)	0.80	0.064
I-T3	1.24	(0.04, 0.08)	0.81	0.059
I-B1	0.2	0.01	0.88	0.068
I-B2	8.9×10^{-2}	2×10^{-3}	0.89	0.034
I-B3	0.34	0.07	0.79	0.01
A-T1	0.47	(0.02,0.03)	0.59	0.047
A-T2	0.66	(0.12,0.05)	0.46	0.076
A-T3	0.97	(0.21,0.03)	0.5	0.049
A-B1	0.51	0.02	0.91	0.063
A-B2	0.59	0.012	0.83	0.026
A-B3	0.85	0.07	0.84	0.082

evaluate NMSE values (in the form of $20\ log(NMSE)\ dB$) for the mapped-pointwise reconstructed images of the pharmacokinetic parameters and volume fractions. Our obtained pointwise NMSEs for k_{pe} (k_{in} in Alacam *et al.*[9]) range from $-31\ dB$ to $-16.9\ dB$ and those for k_{ep} (k_{out} in Alacam *et al.*[9]) range from $-31.3\ dB$ to $-20.94\ dB$ across data SNR levels. The work of Alacam *et al.*[9] reports NMSEs of $-19.77\ dB$ and $-18.49\ dB$ for k_{in} and k_{out} respectively for noiseless data with their synthetic phantoms; they do not report any error values for their volume fractions. This shows that our reconstructions are well within accepted ranges for reconstruction quality.

5 Summary

In this work, we propose a shape based dynamic tomographic reconstruction scheme for fluorescence based pharmacokinetics using a regularized Gauss-Newton filter approach. The contribution of the present work is to represent spatially varying pharmacokinetic parameters, fluorophore con-

Table 5 Values of 20 $log(NMSE)$ dB for the spatial pharmacokinetic parameter and volume fraction values

Phantom	E (k_{pe}) dB	E(k_{ep}) dB	E(v_e) dB	E(v_p) dB	E(k_{elm}) dB
I-T1	-31	-24.22	-17.03	-63.82	-18.55
I-T2	-30.9	-25.07	-17.36	-67.11	-51.5
I-T3	-26.9	-22.01	-10.25	-49.57	-31.11
I-B1	-30	-28.9	-26.2	-65	-44.4
I-B2	-22.6	-28.57	-38.53	-59	-16.8
I-B3	-20.76	-25.74	-20.13	-51	-40.05
A-T1	-28.26	-30.11	-13.7	-60	-61.49
A-T2	-22.61	-24.65	-9.38	-79.29	-21.59
A-T3	-23.5	-20.94	-10.38	-73.3	-35.18
A-B1	-30.49	-28.3	-32.01	-86.1	-39.62
A-B2	-16.92	-31.3	-19.31	-62.73	-39.74
A-B3	-18.55	-26.11	-20.2	-79.38	-42.68

centrations and volume fractions using compactly supported RBF based level-set representations and derive the corresponding shape based Frechet derivatives for time-varying log intensity measurements of the optical signal. An iteratively regularized trust region based Gauss-Newton filter has been proposed to solve this reconstruction problem. It should be noted that we directly reconstruct pharmacokinetic rates, rather than the state equation propagator components (the interim kinetic parameters) as in some previous works.[9,10]

Numerical studies with noisy synthetic data obtained from tumor mimicking numerical phantoms having near/sub-cm dimensions are presented, that validate the proposed scheme. The reconstructions demonstrate good localization and reasonable shape and optical parameter reconstructions, thus demonstrating the good potential of this methodology as an early cancer diagnostic. To obtain a pointwise reconstruction error measure, we mapped our shape and pharmacokinetic parameter reconstructions into pointwise values to compute pointwise-image-NMSEs; comparison

of these pointwise-image-NMSEs with the errors reported in literature for the pharmacokinetic rates show that they are well within acceptable ranges.

The aim of our detailed computational study is to obtain a clear understanding of the numerical characteristics of our proposed algorithm before going to experimental data. Aspects related to application to *in vivo* settings, in addition to the three-dimensional modeling requirement, would be:

1. Characterization of the data-acquisition in terms of limited-data aspects, source-detector configurations(especially depending on region to be interrogated as well as object representation chosen) and detection numerical apertures, detector sensitivity and temporal resolution possible to obtain sufficient data SNRs (for accurate reconstructions, since we observe that in our work the data SNRs would be needed to be above about $30dB$), would be needed while applying the algorithm in actual physical settings.

2. The present results are for scattering dominant media where the diffusion approximation holds as the governing model of light propagation. However for tissues that are absorption dominant over the wavelengths of use, we will have to go in for forward models such as the full RTE[67] or approximations such as the simplified spherical harmonics (SP_n) ones.[38,68]

3. The development of computationally efficient algorithms in 3D and detailed reconstruction studies with respect to image representation and data-acquisition configurations, which is the subject of ongoing work.

Appendix

Expressions of τ_{ij} $i,j=\{1,2\}$ interms of k_ξ, with $\xi=\{ep,pe,elm\}$, are given by equations (58) to (60) (for ease of notations we have omitted the superscript i/o on τ and k-related quantities)

$$\tau_{12}=\frac{4\,k_{ep}\,k_{pe}(\,\mathrm{e}^{\Gamma_2}-\mathrm{e}^{\Gamma_1})}{4\,k_{ep}\,\sqrt{\Xi_1}};\;\;\tau_{21}=-\frac{k_{ep}\,\mathrm{e}^{\Gamma_1}-k_{ep}\,\mathrm{e}^{\Gamma_2}}{\sqrt{\Xi_1}} \tag{58}$$

$$\tau_{11}=\frac{\mathrm{e}^{\Gamma_1}\,\sqrt{\Xi_1}+\mathrm{e}^{\Gamma_2}\,\sqrt{\Xi_1}-k_{elm}\,\mathrm{e}^{\Gamma_1}+k_{elm}\,\mathrm{e}^{\Gamma_2}+k_{ep}\,\mathrm{e}^{\Gamma_1^u}-k_{ep}\,\mathrm{e}^{\Gamma_2}-k_{pe}\,\mathrm{e}^{\Gamma_1}+k_{pe}\,\mathrm{e}^{\Gamma_2}}{2\,\sqrt{\Xi_1}} \tag{59}$$

$$\tau_{22}=\frac{\mathrm{e}^{\Gamma_1}\,\sqrt{\Xi_1}+\mathrm{e}^{\Gamma_2}\,\sqrt{\Xi_1}+k_{elm}\,\mathrm{e}^{\Gamma_1}-k_{elm}\,\mathrm{e}^{\Gamma_2}-k_{ep}\,\mathrm{e}^{\Gamma_1^u}+k_{ep}\,\mathrm{e}^{\Gamma_2}+k_{pe}\,\mathrm{e}^{\Gamma_1}-k_{pe}\,\mathrm{e}^{\Gamma_2}}{2\,\sqrt{\Xi_1}} \tag{60}$$

where Ξ_1, Ξ_2, Γ_1 and Γ_2 are given by the following expressions

$$\Gamma_1=\Xi_2-\frac{t_s\,\sqrt{\Xi_1}}{2};\;\;\Gamma_2=\frac{t_s\,\sqrt{\Xi_1}}{2}+\Xi_2 \tag{61}$$

$$\Xi_1={k_{elm}}^2-2\,k_{elm}\,k_{ep}+2\,k_{elm}\,k_{pe}+{k_{ep}}^2+2\,k_{ep}\,k_{pe}+{k_{pe}}^2 \tag{62}$$

$$\Xi_2=-\frac{k_{elm}\,t_s}{2}-\frac{k_{ep}\,t_s}{2}-\frac{k_{pe}\,t_s}{2} \tag{63}$$

The derivatives of τ_{ij} with respect to k_ξ have expressions which are too large to be included here.

Disclosures

The authors have no relevant financial interests in this article and no potential conflicts of interest to disclose.

References

1 S. R. Meikle, J. C. Matthews, V. J. Cunningham, *et al.*, "Parametric image reconstruction using spectral analysis of PET projection data," *Physics in medicine and biology* **43**(3), 651 (1998). [doi:10.1088/0031-9155/43/3/016].

2 B. Reutter, G. Gullberg, and R. Huesman, "Kinetic parameter estimation from attenuated SPECT projection measurements," *IEEE Transactions on Nuclear Science* **45**(6), 3007–3013 (1998). [doi:10.1109/23.737657].

3 R. H. Huesman, B. W. Reutter, G. L. Zeng, *et al.*, "Kinetic parameter estimation from SPECT cone-beam projection measurements," *Physics in Medicine and Biology* **43**(4), 973 (1998). [doi:10.1088/0031-9155/43/4/024].

4 O. Langer, R. Karch, U. Müller, *et al.*, "Combined PET and microdialysis for in vivo assessment of intracellular drug pharmacokinetics in humans," *Journal of Nuclear Medicine* **46**(11), 1835–1841 (2005).

5 M. E. Kamasak, C. A. Bouman, E. D. Morris, *et al.*, "Direct reconstruction of kinetic parameter images from dynamic PET data," *IEEE transactions on medical imaging* **24**(5), 636–650 (2005). [doi:10.1109/TMI.2005.845317].

6 G. Wang and J. Qi, "Generalized algorithms for direct reconstruction of parametric images from dynamic pet data," *IEEE transactions on medical imaging* **28**(11), 1717–1726 (2009). [doi:10.1109/TMI.2009.2021851].

7 A. B. Milstein, S. Oh, K. J. Webb, *et al.*, "Fluorescence optical diffusion tomography," *Applied Optics* **42**(16), 3081–3094 (2003). [doi:10.1364/AO.42.003081].

8 A. Godavarty, M. J. Eppstein, C. Zhang, *et al.*, "Fluorescence-enhanced optical imaging in large tissue volumes using a gain-modulated ICCD camera," *Physics in Medicine and Biology* **48**(12), 1701 (2003). [doi:10.1088/0031-9155/48/12/303].

9 B. Alacam and B. Yazici, "Direct reconstruction of pharmacokinetic-rate images of optical fluorophores from NIR measurements," *IEEE transactions on medical imaging* **28**(9), 1337–1353 (2009). [doi:10.1109/TMI.2009.2015294].

10 X. Wang, Y. Zhang, L. Zhang, *et al.*, "Direct reconstruction in CT-analogous pharmacokinetic diffuse fluorescence tomography: two-dimensional simulative and experimental validations," *Journal of biomedical optics* **21**(4), 046007–046007 (2016). [doi:10.1117/1.JBO.21.4.046007].

11 X. Zhang, F. Liu, S. Zuo, *et al.*, "Reconstruction of fluorophore concentration variation in dynamic fluorescence molecular tomography," *IEEE Transactions on Biomedical Engineering* **62**(1), 138–144 (2015). [doi:10.1109/TBME.2014.2342293].

12 X. Liu, B. Zhang, J. Luo, *et al.*, "4-D reconstruction for dynamic fluorescence diffuse optical tomography," *IEEE transactions on medical imaging* **31**(11), 2120–2132 (2012). [doi:10.1109/TMI.2012.2213828].

13 G. Zhang, F. Liu, H. Pu, *et al.*, "A direct method with structural priors for imaging pharmacokinetic parameters in dynamic fluorescence molecular tomography," *IEEE Transactions on Biomedical Engineering* **61**(3), 986–990 (2014). [doi: 10.1109/TBME.2013.2292714].

14 X. Zhang, F. Liu, S. Zuo, *et al.*, "Fast reconstruction of fluorophore concentration varia-

tion based on the derivation of the diffusion equation," *JOSA A* **32**(11), 1993–2001 (2015). [doi:10.1364/JOSAA.32.001993].

15 J. A. Jacquez, *Compartmental Analysis in Biology and Medicine, Kinetics of Distribution of Tracer-Labeled Materials*, New York: Elsevier (1972).

16 Y. Kwon, *Handbook of essential pharmacokinetics, pharmacodynamics and drug metabolism for industrial scientists*, Springer Science & Business Media, New York (2001). [doi:10.1007/b112416].

17 S. E. Rosenbaum, *Basic pharmacokinetics and pharmacodynamics: An integrated textbook and computer simulations*, John Wiley & Sons (2016).

18 H. Sun, J. M. Collins, T. J. Mangner, *et al.*, "Imaging the pharmacokinetics of [F-18] FAU in patients with tumors: PET studies," *Cancer chemotherapy and pharmacology* **57**(3), 343–348 (2006). [doi:10.1007/s00280-005-0037-0].

19 M. Gurfinkel, A. B. Thompson, W. Ralston, *et al.*, "Pharmacokinetics of ICG and HPPH-car for the detection of normal and tumor tissue using fluorescence, near-infrared reflectance imaging: a case study," *Photochemistry and photobiology* **72**(1), 94–102 (2000). [doi:10.1562/0031-8655(2000)0720094POIAHC2.0.CO2].

20 A. B. Milstein, K. J. Webb, and C. A. Bouman, "Estimation of kinetic model parameters in fluorescence optical diffusion tomography," *JOSA A* **22**(7), 1357–1368 (2005). [doi:10.1364/JOSAA.22.001357].

21 B. Alacam, B. Yazici, X. Intes, *et al.*, "Pharmacokinetic-rate images of indocyanine green for breast tumors using near-infrared optical methods," *Physics in medicine and biology* **53**(4), 837 (2008). [doi:10.1088/0031-9155/53/4/002].

22 X. Wang, L. Wu, X. Yi, *et al.*, "Performance enhancement of pharmacokinetic diffuse fluorescence tomography by use of adaptive extended Kalman filtering," *Computational and mathematical methods in medicine* **2015** (2015). [doi:10.1155/2015/739459].

23 G. Zhang, H. Pu, W. He, *et al.*, "Bayesian framework based direct reconstruction of fluorescence parametric images.," *IEEE Trans. Med. Imaging* **34**(6), 1378–1391 (2015). [doi:10.1109/TMI.2015.2394476].

24 G. Zhang, H. Pu, W. He, *et al.*, "Full-direct method for imaging pharmacokinetic parameters in dynamic fluorescence molecular tomography," *Applied Physics Letters* **106**(8), 081110 (2015). [doi:10.1063/1.4913690].

25 G. Zhang, F. Liu, B. Zhang, *et al.*, "Imaging of pharmacokinetic rates of indocyanine green in mouse liver with a hybrid fluorescence molecular tomography/x-ray computed tomography system," *Journal of biomedical optics* **18**(4), 040505 (2013). [doi:10.1117/1.JBO.18.4.040505].

26 S. C. Davis, H. Dehghani, J. Wang, *et al.*, "Image-guided diffuse optical fluorescence tomography implemented with laplacian-type regularization," *Optics express* **15**(7), 4066–4082 (2007). [doi:10.1364/OE.15.004066].

27 F. Santosa, "A level-set approach for inverse problems involving obstacles," *ESAIM: Control, Optimisation and Calculus of Variations* **1**, 17–33 (1996). [doi:10.1051/cocv:1996101].

28 M. E. Kilmer, E. L. Miller, A. Barbaro, *et al.*, "Three-dimensional shape-based imaging of absorption perturbation for diffuse optical tomography," *Applied Optics* **42**(16), 3129–3144 (2003). [doi:10.1364/AO.42.003129].

29 A. D. Zacharopoulos, S. R. Arridge, O. Dorn, *et al.*, "Three-dimensional reconstruction of

shape and piecewise constant region values for optical tomography using spherical harmonic parametrization and a boundary element method," *Inverse Problems* **22**(5), 1509 (2006). [doi:10.1088/0266-5611/22/5/001].

30 O. Dorn and D. Lesselier, "Level set methods for inverse scattering," *Inverse Problems* **22**(4), R67 (2006). [doi:10.1088/0266-5611/22/4/R01].

31 S. R. Arridge, O. Dorn, V. Kolehmainen, *et al.*, "Parameter and structure reconstruction in optical tomography," in *Journal of Physics: Conference Series*, **135**(1), 012001, IOP Publishing (2008). [doi:10.1088/1742-6596/135/1/012001].

32 N. Naik, J. Eriksson, P. de Groen, *et al.*, "A nonlinear iterative reconstruction and analysis approach to shape-based approximate electromagnetic tomography," *IEEE Transactions on Geoscience and Remote Sensing* **46**(5), 1558–1574 (2008). [doi:10.1109/TGRS.2008.916077].

33 O. Dorn and D. Lesselier, "Level set methods for inverse scattering- some recent developments," *Inverse Problems* **25**(12), 125001 (2009). [doi:10.1088/0266-5611/25/12/125001].

34 F. Larusson, P. G. Anderson, E. Rosenberg, *et al.*, "Parametric estimation of 3D tubular structures for diffuse optical tomography," *Biomedical optics express* **4**(2), 271–286 (2013). [doi:10.1364/BOE.4.000271].

35 L. Wu, W. Wan, X. Wang, *et al.*, "Shape-parameterized diffuse optical tomography holds promise for sensitivity enhancement of fluorescence molecular tomography," *Biomedical optics express* **5**(10), 3640–3659 (2014). [doi:10.1364/BOE.5.003640].

36 M. E. Kilmer, E. L. Miller, D. Boas, *et al.*, "A shape-based reconstruction technique for DPDW data," *Optics Express* **7**(13), 481–491 (2000). [doi:10.1364/OE.7.000481].

37 A. Aghasi, M. Kilmer, and E. L. Miller, "Parametric level set methods for inverse problems," *SIAM Journal on Imaging Sciences* **4**(2), 618–650 (2011). [doi:10.1137/100800208].

38 N. Naik, N. Patil, Y. Yadav, *et al.*, "Fully nonlinear SP_3 approximation based fluorescence optical tomography," *IEEE transactions on medical imaging* **36**(11), 2308–2318 (2017). [doi:10.1109/TMI.2017.2718028].

39 N. Naik, R. Beatson, and J. Eriksson, "Radial-basis-function level-set-based regularized Gauss–Newton-filter reconstruction scheme for dynamic shape tomography," *Applied optics* **53**(29), 6872–6884 (2014). [doi:10.1364/AO.53.006872].

40 X. Zhang, J. Zhang, J. Bai, *et al.*, "Shape-based reconstruction of dynamic fluorescent yield with a level set method," *Biomedical engineering online* **15**(1), 6 (2016). [doi:10.1186/s12938-016-0124-y].

41 O. Gottam, N. Naik, and S. Gambhir, "Shape based pharmacokinetic fluorescence optical tomography," in *Biomedical Imaging and Sensing Conference*, **10711**, 107110M, International Society for Optics and Photonics (2018). [doi:10.1117/12.2319358].

42 X. Intes, J. Ripoll, Y. Chen, *et al.*, "In vivo continuous-wave optical breast imaging enhanced with indocyanine green," *Medical physics* **30**(6), 1039–1047 (2003). [doi:10.1118/1.1573791].

43 D. J. Cuccia, F. Bevilacqua, A. J. Durkin, *et al.*, "In vivo quantification of optical contrast agent dynamics in rat tumors by use of diffuse optical spectroscopy with magnetic resonance imaging coregistration," *Applied optics* **42**(16), 2940–2950 (2003). [doi:10.1364/AO.42.002940].

44 B. Alacam, B. Yazici, X. Intes, *et al.*, "Extended Kalman filtering for the mod-

eling and analysis of ICG pharmacokinetics in cancerous tumors using NIR optical methods," *IEEE transactions on biomedical engineering* **53**(10), 1861–1871 (2006). [doi:10.1109/TBME.2006.881796].

45 J. A. Jacquez, *Compartmental analysis in biology and medicine.*, Amesterdam (1972).

46 V. Ntziachristos, A. Yodh, M. Schnall, *et al.*, "Concurrent MRI and diffuse optical tomography of breast after indocyanine green enhancement," *Proceedings of the National Academy of Sciences* **97**(6), 2767–2772 (2000). [doi:10.1073/pnas.040570597].

47 D. A. Hansen, A. M. Spence, T. Carski, *et al.*, "Indocyanine green (ICG) staining and demarcation of tumor margins in a rat glioma model," *Surgical neurology* **40**(6), 451–456 (1993). [doi:10.1016/0090-3019(93)90046-4].

48 T. Ishizawa, N. Fukushima, J. Shibahara, *et al.*, "Real-time identification of liver cancers by using indocyanine green fluorescent imaging," *Cancer* **115**(11), 2491–2504 (2009). [doi:10.1002/cncr.24291].

49 M.-Y. Su, A. Mühler, X. Lao, *et al.*, "Tumor characterization with dynamic contrast–enhanced MRI using mr contrast agents of various molecular weights," *Magnetic resonance in medicine* **39**(2), 259–269 (1998). [doi:10.1002/mrm.1910390213].

50 S. S. Jambhekar and P. J. Breen, *Basic pharmacokinetics*, vol. 76, Pharmaceutical Press London, UK: (2009).

51 D. L. Buckley, "Uncertainty in the analysis of tracer kinetics using dynamic contrast-enhanced T1-weighted MRI," *Magnetic resonance in medicine* **47**(3), 601–606 (2002). [doi:10.1002/mrm.10080].

52 P. S. Tofts, G. Brix, D. L. Buckley, *et al.*, "Estimating kinetic parameters from dynamic contrast-enhanced T1-weighted MRI of a diffusable tracer: standardized quantities and symbols," *Journal of magnetic resonance imaging* **10**(3), 223–232 (1999). [doi:10.1002/(SICI)1522-2586(199909)10:3¡223::AID-JMRI2¿3.0.CO;2-S].

53 C.-T. Chen, *Linear system theory and design*, Oxford University Press, Inc. (1995).

54 F. Fedele, J. Laible, and M. Eppstein, "Coupled complex adjoint sensitivities for frequency-domain fluorescence tomography: theory and vectorized implementation," *Journal of Computational Physics* **187**(2), 597–619 (2003). [doi:10.1016/S0021-9991(03)00150-5].

55 H. Wendland, *Scattered data approximation*, vol. 17, Cambridge university press (2004). [doi:10.1017/CBO9780511617539].

56 T. F. Chan and L. A. Vese, "Active contours without edges," *IEEE Transactions on image processing* **10**(2), 266–277 (2001). [doi:10.1109/83.902291].

57 D. Simon, *Optimal state estimation: Kalman, H infinity, and nonlinear approaches*, John Wiley & Sons (2006). [doi:10.1002/0470045345].

58 N. Morrison, *Tracking filter engineering: the Gauss-Newton and polynomial filters*, The Institution of Engineering and Technology (2012). [doi:10.1049/PBRA023E].

59 M. Schweiger, S. R. Arridge, and I. Nissilä, "Gauss–Newton method for image reconstruction in diffuse optical tomography," *Physics in medicine and biology* **50**(10), 2365 (2005). [doi:10.1088/0031-9155/50/10/013].

60 J. Nocedal and S. Wright, "Numerical optimization, series in operations research and financial engineering," *Springer, New York, USA, 2006* (2006). [doi:10.1007/978-0-387-40065-5].

61 E. de Sturler and M. E. Kilmer, "A regularized Gauss–Newton trust region approach to imaging in diffuse optical tomography," *SIAM Journal on Scientific Computing* **33**(5), 3057–3086 (2011). [doi:10.1137/100798181].

62 A. R. Conn, N. I. Gould, and P. L. Toint, *Trust region methods*, vol. 1, Siam (2000). [doi:10.1137/1.9780898719857].

63 M. J. Eppstein, D. E. Dougherty, T. L. Troy, *et al.*, "Biomedical optical tomography using dynamic parameterization and Bayesian conditioning on photon migration measurements," *Applied optics* **38**(10), 2138–2150 (1999). [doi:10.1364/AO.38.002138].

64 M. Schweiger, S. Arridge, M. Hiraoka, *et al.*, "The finite element method for the propagation of light in scattering media: boundary and source conditions," *Medical physics* **22**(11), 1779–1792 (1995). [doi:10.1118/1.597634].

65 M. J. Eppstein, F. Fedele, J. Laible, *et al.*, "A comparison of exact and approximate adjoint sensitivities in fluorescence tomography," *IEEE Transactions on Medical Imaging* **22**(10), 1215–1223 (2003). [doi: 10.1109/TMI.2003.818165].

66 F. Larusson, S. Fantini, and E. L. Miller, "Parametric level set reconstruction methods for hyperspectral diffuse optical tomography," *Biomedical optics express* **3**(5), 1006–1024 (2012). [doi:10.1364/BOE.3.001006].

67 H. K. Kim and A. H. Hielscher, "A pde-constrained sqp algorithm for optical tomography based on the frequency-domain equation of radiative transfer," *Inverse Problems* **25**(1), 015010 (2008). [doi:10.1088/0266-5611/25/1/015010].

68 A. D. Klose and E. W. Larsen, "Light transport in biological tissue based on the simplified

spherical harmonics equations," *Journal of Computational Physics* **220**(1), 441–470 (2006). [doi:10.1016/j.jcp.2006.07.007].